

Direct numerical simulation of turbulent channel flow over random rough surfaces

Rong Ma¹, Karim Alamé¹ and Krishnan Mahesh^{1†}

¹Department of Aerospace Engineering and Mechanics, University of Minnesota, Minneapolis, MN 55455, USA

(Received xx; revised xx; accepted xx)

Direct numerical simulation (DNS) of flow in a turbulent channel with a random rough wall is performed at $Re_\tau = 400$ and 600. The roughness geometry corresponds to the experiments of Flack and Schultz (personal communication). The rough surface is used on the bottom wall of the channel. DNS of a smooth channel flow and a rod-roughened channel flow are also performed at $Re_\tau = 400$ for validation and comparison. The skin friction coefficient of the random-rough channel shows good agreement with the experimental results of Flack and Schultz. Due to the roughness, the slip velocity on the rough wall increases while the mean velocity decreases in the log-law region. The streamwise and spanwise velocity fluctuations are enhanced near the rough wall. The pressure fluctuations show a significant increase in the roughness layer and exhibit a good collapse with the smooth wall in the outer layer. The streamwise mean momentum balance shows that pressure and viscous stress gradients are induced in the roughness layer, and the gradients are amplified at higher Re_τ . The statistics of wall-shear stress fluctuations in the peak (above the mean height location) and valley (below the mean height location) regions are examined. The results indicate that reverse flow mainly occurs in the valley regions of the random roughness, and is enhanced at higher Re_τ , but is not as strong as the recirculation within the cavities in the rod-roughened channel. The probability distribution function of wall-shear stress shows a better collapse after subtracting the mean and normalizing by the root-mean-squared value. The distribution tail is widened by the random roughness, implying that the probability of extreme events is increased. The probability of extreme events in the random-rough channel increases with increasing Re_τ , in accordance with previous studies on smooth-wall flows. The wall-shear stress spectra show that the low and medium frequencies contain more energy while the high frequencies contain less energy, compared to those in the smooth channel.

Key words: Authors should not enter keywords on the manuscript, as these must be chosen by the author during the online submission process and will then be added during the typesetting process

1. Introduction

Wall roughness has important effects on turbulent flows, especially at high Reynolds numbers. Surfaces with riblets are designed to achieve drag reduction (Bechert *et al.* 1997). Sediment and vegetation canopies impose local effects in the near-bed region (Mignot *et al.* 2009). “Urban roughness” has influence on the urban climate (Cheng &

† Email address for correspondence: kmahesh@umn.edu

Castro 2002). Many processes such as erosion, pitting (Bons *et al.* 2001) and bio-fouling (Kirschner & Brennan 2012) can produce complex surface topographies, which in turn, give rise to increased fuel consumption and reduced efficiency in engineering systems.

Raupach *et al.* (1991) and Jiménez (2004) have summarized roughness effects on turbulent boundary layers, including the offset of mean velocity profile, the enhancement of intensities, and the modification of flow structures. The roughness function $\Delta U^+ = \Delta U u_\tau / \nu$, where ΔU is the mean velocity difference in the logarithmic layer between the smooth and rough walls, u_τ is the average friction velocity and ν is the kinematic viscosity of the fluid. Based on the early experiments by Nikuradse (1933) for sand-grain roughness, three flow regimes were defined for rough-wall flows by using ΔU^+ as a function of k^+ , the roughness scale in viscous units. When k^+ is small, ΔU^+ is nearly zero, i.e., the flow is hydraulically smooth. In this regime, the viscosity damps out the perturbations caused by the roughness. The flow becomes transitionally rough as k^+ increases, where the skin friction has contributions from both viscous drag and form drag. As k^+ further increases, the roughness function reaches a linear asymptote, and the flow is considered fully rough.

The roughness scale is an important parameter and different definitions exist, such as the average roughness height k_a^+ , the peak-to-valley roughness height k_t^+ , or the equivalent sandgrain roughness height k_s^+ . According to Nikuradse (1933), k_s^+ is determined by fitting a roughness height to match a measured pressure drop in experiments. Jiménez (2004) and Flack & Schultz (2010) suggest that k_s^+ can provide a better collapse of ΔU^+ in the fully rough regime for various roughness types. Correlations to predict the frictional drag for rough surfaces are summarized by Flack & Schultz (2010), who also propose a new correlation to predict k_s in the fully rough regime. However, the data of ΔU^+ in the transitionally rough regime shows considerable scatter for different roughness types. Flack & Schultz (2010) note that the transitionally rough regime is the least understood, and the parameter ranges that determine the transitionally rough regime remain unknown for most roughness types. Barros *et al.* (2017) measured the skin friction for systematically-controlled random rough surfaces and emphasized that the understanding of the frictional drag in the transitionally rough regime is poor.

Surface roughness can be classified as regular or irregular (random) roughness. Many experimental and computational studies have been performed on regular roughness, for example, ribbed, cubed or spherical surfaces (Schlichting 1936; Bechert *et al.* 1997; Orlandi & Leonardi 2006; Lee *et al.* 2011). With the development of advanced experimental and computational methodologies, irregular rough surfaces have been paid more attention in recent years. The effects of irregular rough surfaces on the mean quantities in turbulent boundary layers including velocity profiles, turbulent intensities, turbulent kinetic energy, two-point correlations, etc, were investigated (Mejia-Alvarez & Christensen 2010; Cardillo *et al.* 2013; Busse *et al.* 2015; Anderson *et al.* 2015). Yuan & Piomelli (2014) performed large-eddy simulations on turbulent channel flows for realistic surfaces replicated from turbine blades and examined the existing correlations to predict k_s . Mean momentum balance (MMB) was analysed in rough-wall turbulent boundary layers by Mehdi *et al.* (2010). They found that the main features of the layer structure in smooth-wall flows also existed in rough-wall boundary layers, however, the experimental data were quite scattered, which made it difficult to examine the properties of the MMB. Yuan & Jouybari (2018) used the double-averaging decomposition to investigate how the range of roughness scales affects the momentum and energy balance. Flack *et al.* (2005) and Wu & Christensen (2007) found that for rough surfaces with small roughness height (compared to the boundary layer thickness or channel half-height), turbulent statistics in the outer layer are not affected by the roughness (“outer-layer similarity”). The near-

wall region where the roughness effects on the mean flow are significant is termed the “roughness sublayer”. Busse *et al.* (2017) investigated Re dependence of the near-wall flow in the vicinity of and within the rough surfaces. They characterized the near-wall flow by estimating the thickness of the roughness sublayer and examining the probability distribution of the reverse flow. Jelly & Busse (2018) studied the dependence of the near-wall flow on higher-order surface parameters, such as skewness, by evaluating the influence on the roughness function.

Past work has mainly focused on the mean flow and the scaling of velocity statistics over rough surfaces. Less is known about the statistics of wall-shear stress fluctuations, which are closely related to drag, sound radiation and structural vibration. For smooth-wall flows, numerous experiments were conducted to measure the root-mean-square (rms) wall-shear stress fluctuations $\tau_{x,rms}$ (Eckelmann 1974; Chambers *et al.* 1983; Madavan *et al.* 1985). Alfredsson *et al.* (1988) found that the previous experimental results of $\tau_{x,rms}$ have a large scatter due to the difficulties in measurements. Experiments were carried out using near-wall hot-wire probes by Khoo *et al.* (2001) to investigate the probability distribution function (p.d.f.) of wall-shear stress and streamwise velocity fluctuations. The similarity in p.d.f. indicates the high correlation between τ and u .

DNS has been used to investigate the wall-shear stress fluctuations in smooth wall-bounded flows. Abe *et al.* (2004) performed DNS to investigate the effects of very large-scale structures on the wall-shear stress fluctuations. Hu *et al.* (2006) conducted DNS to study the Re dependence of wall-shear stress spectra in a turbulent plane channel flow. Örlü & Schlatter (2011) combined DNS data with experimental results to examine the Re dependence of wall-shear stress fluctuations. Diaz-Daniel *et al.* (2017) investigated the statistics of wall-shear stress fluctuations in a turbulent boundary layer and their effects on velocity fluctuations. Similar studies on rough-wall flows are scarce. The complex surface geometries cause local variation in wall-pressure and wall-shear stress, making direct measurements challenging. For example, Meyers *et al.* (2015) studied the wall-pressure spectrum over rough walls experimentally. They measured pressure at one streamwise and several spanwise locations, and carefully placed microphones to avoid the direct influence of the roughness on the measurements. Wall-shear stress measurements are even more challenging. DNS of such flow, if possible, can overcome these difficulties. Simulations are challenged by the complex random-rough geometry and the faithful representation of the experimental three-dimensional (3D) surface-scanned data. Also, the present random rough surface has very small roughness scales, meaning that high resolution is required to resolve the near-wall flow which impacts the Re that is feasible.

In the present work, DNS of turbulent channel flow over random rough surfaces is performed at two Re_τ . The objectives of our work are to (i) demonstrate the predictive capability of DNS for turbulent flows over random rough surfaces, (ii) explore the roughness effects and Re_τ dependence on the mean properties and turbulent statistics, and (iii) characterize the wall-shear stress fluctuations on random rough surfaces. The numerical method and validations of the DNS solver are introduced in §2. The surface processing and the problem setup are described in §3. The results and discussions are presented in §4. Finally, a summary is provided in §5.

2. Simulation details

2.1. Numerical method

The governing equations are solved using the finite volume algorithm developed by Mahesh *et al.* (2004) for the incompressible Navier-Stokes equations. The governing

Turbulent channel flow	Case	Re_τ	$N_x \times N_y \times N_z$	$L_x \times L_y \times L_z$	Δx^+	Δz^+	Δy_{min}^+	Δy_{max}^+
Smooth wall	SW	400	$768 \times 320 \times 384$	$2\pi \times 2.03 \times \pi$	3.27	3.27	0.85	5.48
Rod-roughened wall	RRW	400	$768 \times 320 \times 320$	$6.528 \times 2 \times \pi$	3.40	3.92	0.85	5.48

TABLE 1. Simulation parameters for DNS of the validation cases.

equations for the momentum and continuity equations are given by the Navier-Stokes equations:

$$\frac{\partial u_i}{\partial t} + \frac{\partial}{\partial x_j} (u_i u_j) = -\frac{\partial p}{\partial x_i} + \nu \frac{\partial}{\partial x_j} \left(\frac{\partial u_i}{\partial x_j} + \frac{\partial u_j}{\partial x_i} \right) + K_i, \quad (2.1)$$

$$\frac{\partial u_i}{\partial x_i} = 0, \quad (2.2)$$

where u_i and x_i are the i -th component of the velocity and position vectors respectively, p denotes pressure, ν is the kinematic viscosity of the fluid and K_i is the body force. The algorithm is robust and emphasizes discrete kinetic energy conservation in the inviscid limit which enables it to simulate high-Re flows without adding numerical dissipation. A predictor-corrector methodology is used where the velocities are first predicted using the momentum equation, and then corrected using the pressure gradient obtained from the Poisson equation yielded by the continuity equation. The Poisson equation is solved using a multigrid pre-conditioned conjugate gradient method (CGM) using the Trilinos libraries (Sandia National Labs). The implicit time advancement uses the Crank-Nicholson discretization with a linearisation of the convective terms and a successive over relaxation (SOR) method.

The surface is represented by obstacle cells which are masked out. At the beginning of the simulation, the fluid and obstacle cells are flagged accordingly:

$$mask = \begin{cases} 1, & \text{if fluid cell} \\ 0, & \text{if obstacle cell} \end{cases}; \quad (2.3)$$

The wetted masked cells (cells that share a face between a fluid and obstacle cell) enforce a zero face-normal velocity. The cell-centred velocities satisfy a no-slip boundary condition, with the exception of corner cells that take a weighted average of the neighbouring cell-centred values.

2.2. Validation

The DNS code is validated against a smooth turbulent channel flow, as well as a rod-roughened turbulent channel flow (Table 1). The smooth channel flow at $Re_\tau = 400$ (Case SW) is used as the baseline, and compared to Moser *et al.* (1999) at $Re_\tau = 395$. The streamwise mean velocity U is normalized by the average friction velocity u_τ , and the Reynolds stresses are normalized by u_τ^2 . The wall-normal distance y is presented in the inner coordinate. Good agreement of the mean velocity and Reynolds stresses profiles is shown in figure 1.

Then, the DNS code is employed to simulate the turbulent channel flow over rod-roughened walls at $Re_\tau = 400$ (Case RRW). Both top and bottom walls are roughened by 24 square rods with a roughness height k which is 1.7% of the channel height. The

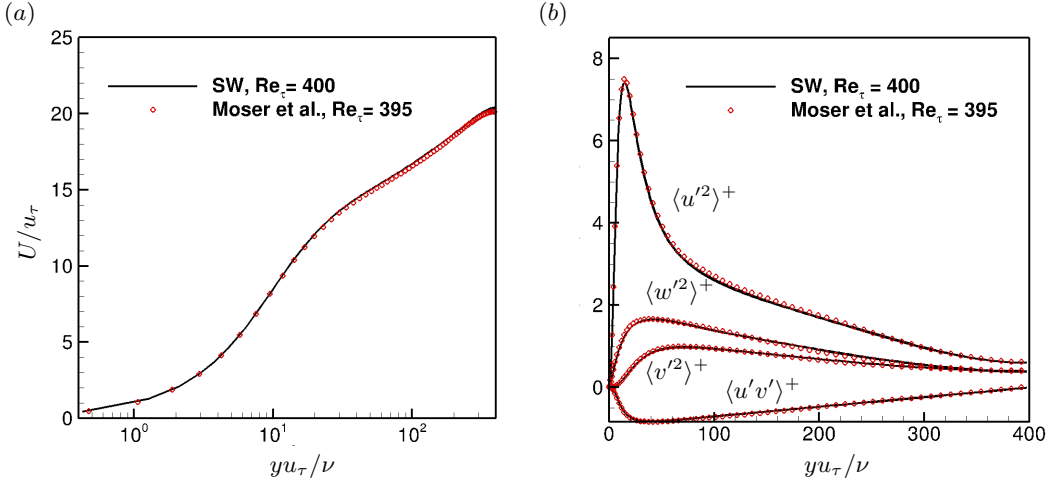


FIGURE 1. DNS of a smooth channel flow at $Re_\tau = 400$ compared to the DNS of Moser *et al.* (1999): (a) mean velocity profile and (b) Reynolds stresses in the inner coordinate.

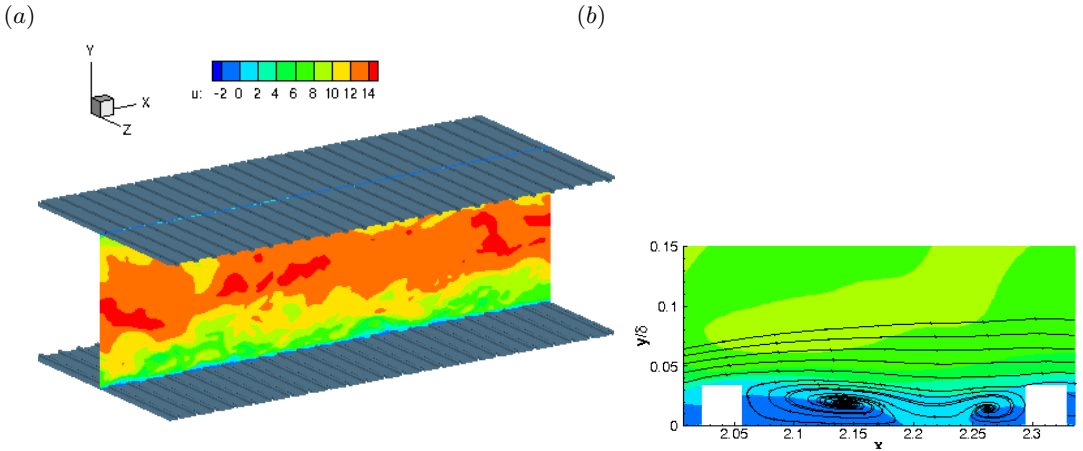


FIGURE 2. DNS of a rod-roughened channel flow at $Re_\tau = 400$: (a) flow configuration with an xy plane of the streamwise velocity field and (b) streamline pattern at the vicinity of the rods.

pitch-to-height ratio λ/k is 8, where λ denotes the pitch, i.e. the summation of the rod height and the streamwise distance between two adjacent rods. The corresponding roughness height in viscous length scale k^+ is equal to 13.6. The flow regime is classified as the transitionally rough regime, according to Ligrani & Moffat (1986). Figure 2(a) demonstrates the flow configuration and the roughness shape. A coordinate system is adopted in which x is aligned with the primary flow direction, y is normal to the walls, and z is parallel to the roughness crests. Periodic boundary conditions are used in the streamwise and spanwise directions and no-slip conditions are imposed at the solid surfaces. Non-uniform grids are used in the wall-normal direction while uniform grids are used in both streamwise and spanwise directions. The domain size and the resolution in wall-normal directions are practically equivalent to Case SW. The spanwise resolution is coarser than the streamwise resolution since the roughness is uniform in the spanwise direction.

The mean velocity and Reynolds stresses at $x/\lambda = 0.312$ are compared to Ashrafian

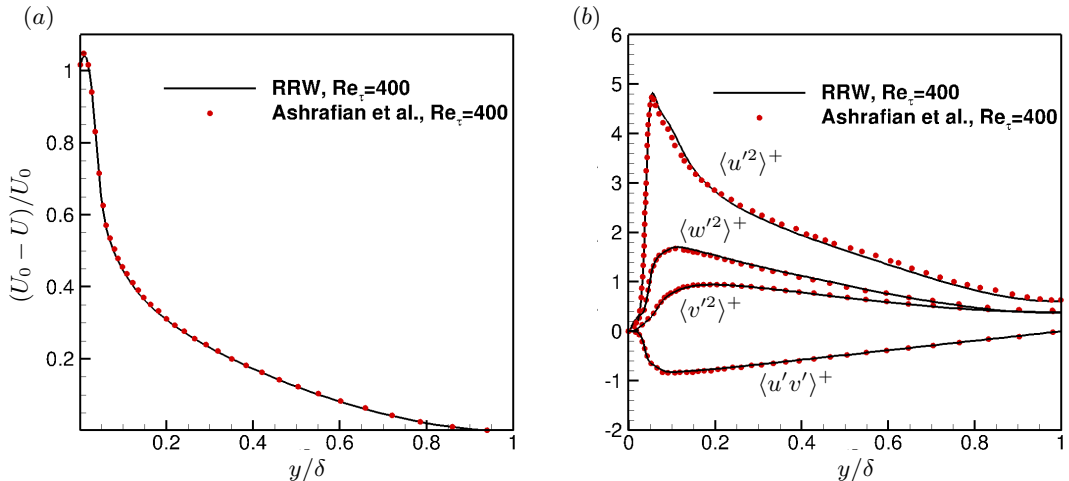


FIGURE 3. DNS of a rod-roughened channel flow at $Re_\tau = 400$ compared to the DNS of Ashrafian *et al.* (2004): (a) defect profiles scaled with centerline velocity U_0 at $x/\lambda = 0.312$ and (b) Reynolds stresses in the outer layer coordinate at $x/\lambda = 0.312$.

et al. (2004) in figure 3. This selected position is located at the focal point of the primary recirculation downstream of the roughness element, as shown in figure 2(b). Figure 3(a) shows the mean velocity profiles scaled with the centerline velocity U_0 . The variation of the Reynolds stresses normalized by u_τ^2 at $x/\lambda = 0.312$ is shown in figure 3(b). Both the mean velocity and Reynolds stresses profiles are presented in the outer layer coordinate, where y is normalized by the channel half-height δ . The results show good agreement with Ashrafian *et al.* (2004).

3. Problem setup

3.1. Surface data processing

The random rough surfaces investigated in this work are processed from rough surface tiles which are scanned and provided by Flack and Schultz (personal communication). The details of surface tile generation in the experiments are presented by Barros *et al.* (2017).

Four rough tiles with the same k_{rms} around $88\mu m$ are used to produce the rough bottom wall for the simulations. The original tile is a rectangular patch of roughness of size $50mm$ by $15mm$. The number of pixels in the length and width corresponds to the number of nodes in the streamwise and spanwise directions. Based on the requirement of the streamwise and spanwise resolution in Case R400, each rough tile is interpolated into grids size of 489×147 . In Case R600 and R400f, tiles are interpolated into finer grids according to the finer resolution. Then, the interpolated rough tiles are rotated in a random orientation and tiled to achieve a domain size of $2\pi\delta \times \pi\delta$, where δ is the channel half-height. The test section height is $25 mm$ in the turbulent channel facility, as mentioned in Barros *et al.* (2017), thus the length, width of the rough surface and the roughness height are all scaled by the channel half-height of $12.5 mm$.

The values of the roughness height are interpolated to the cell centres. These interpolated roughness heights are then written into a new file, which presents the final rough surface applied to the simulation. The characteristic parameters of the rough surface in Case R400 before scaling are compared to those of the original tiles, and

Parameter	Description	Tile 1	Tile 2	Tile 3	Tile 4	Average	Rough surface
k_a	Average Roughness Height	0.0691	0.0698	0.0700	0.0718	0.0702	0.0692
k_{rms}	RMS Roughness Height	0.0862	0.0875	0.0878	0.0892	0.0877	0.0865
k_t	Maximum Peak to Valley Height	0.703	0.692	0.696	0.729	0.705	0.745
Sk	Skewness	-0.021	-0.083	-0.073	-0.080	-0.064	-0.053
Ku	Kurtosis (Flatness)	2.932	2.985	2.974	2.812	2.926	2.933
ES_x	Effective Slope of Roughness in x	0.360	0.390	0.372	0.370	0.373	0.265
ES_z	Effective Slope of Roughness in z	0.359	0.392	0.370	0.371	0.373	0.265

TABLE 2. Surface statistics of the processed random rough surface in Case R400, compared to those of original tiles. The roughness height is in mm .

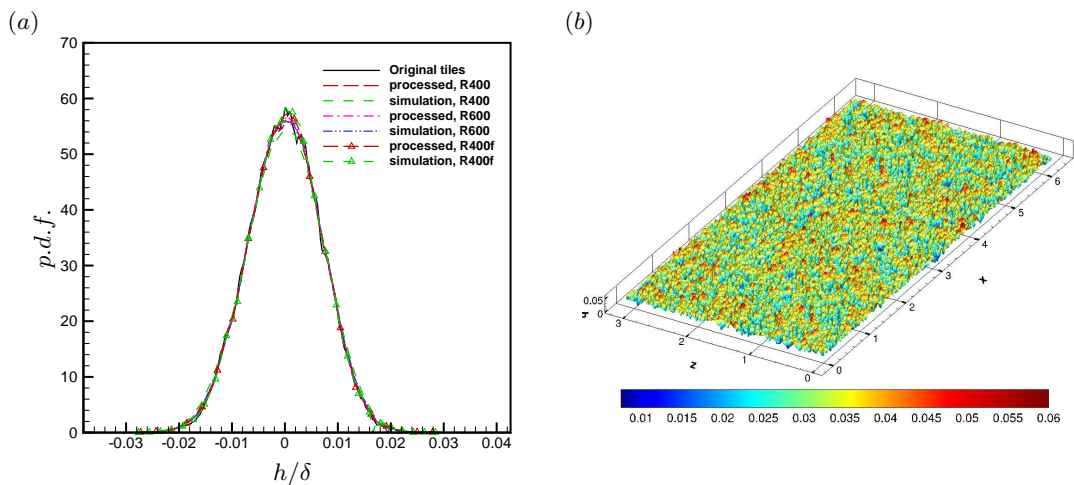


FIGURE 4. (a) The probability density function (p.d.f.) of the height normalized by the channel half-height δ for the processed rough surface and the rough surface applied to the simulations, compared to the original surface tiles; (b) Illustration of the rough surface. The contour legend describes the height of the surface profile normalized by δ .

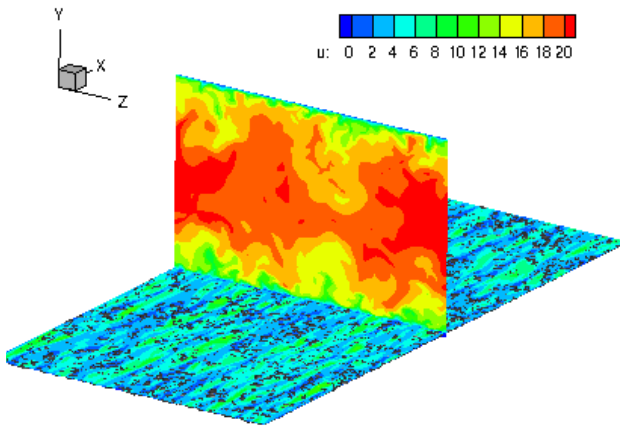
good agreement is shown in table 2. The probability distribution function (p.d.f.) of the processed rough surface and the rough surface in the simulations are compared to the original tiles in figure 4(a). The good agreement in p.d.f. suggests that the rough surface is processed appropriately and the surface statistics are not changed significantly. Figure 4(b) visualizes the rough surface.

3.2. Problem description

Simulations are performed in turbulent channel flows at $Re_\tau = u_\tau \delta / \nu = 400$ and 600, where u_τ is the wall friction velocity, $\delta = (L_y - d)/2$ is the channel half-height and d is the location of the virtual origin. The rough surface only exists on the bottom wall. The virtual origin is set to be the arithmetic mean elevation of the roughness. The channel flows are simulated with no-slip boundary conditions on the wall and periodic boundary conditions in the streamwise and spanwise directions. Domains and grid details are shown in table 3. The random-rough case at $Re_\tau = 400$ is denoted by Case R400 and the random-rough case at $Re_\tau = 600$ is Case R600. k_s^+ is equal to 5.12 for Case R400 and 7.68 for Case

Case	Re_τ	$N_x \times N_y \times N_z$	$L_x \times L_y \times L_z$	Δx^+	Δz^+	Δy_{min}^+	Δy_{max}^+
R400	400	$768 \times 320 \times 384$	$2\pi\delta \times 2.03\delta \times \pi\delta$	3.27	3.27	0.85	5.64
R600	600	$1154 \times 540 \times 577$	$2\pi\delta \times 2.03\delta \times \pi\delta$	3.27	3.27	0.43	5.64
R400f	400	$667 \times 540 \times 400$	$4\delta \times 2.03\delta \times 2.4\delta$	2.40	2.40	0.28	3.80

TABLE 3. Simulation parameters for DNS of the random-rough cases.

FIGURE 5. Simulation of the turbulent random-rough channel flows at $Re_\tau = 400$, illustrated by the streamwise velocity field at x plane and y plane at $y^+ = 6$.

R600. The simulation time step Δt is 5×10^{-4} . In order to achieve statistical convergence, mean quantities and statistics were averaged over a period $T = 50$. An illustration of the turbulent random-rough channel flow at $Re_\tau = 400$ is shown in figure 5. A cross section and a plane at $y^+ = 6$ of the turbulent channel flow are visualized by the instantaneous streamwise velocity field.

3.3. Grid convergence

A grid convergence study is performed for the same rough surface at same Re_τ denoted by Case R400f. The simulation details are listed in table 3. A smaller domain is used for the grid-refined simulation to reduce the computational cost. Past work on smooth turbulent channel (Lozano-Durán & Jiménez 2014) and turbulent channel with urban-like cubical obstacles (Coceal *et al.* 2006) suggest that a domain size of $L_x \times L_z = 4\delta \times 2.4\delta$ is sufficient for obtaining mean and turbulent statistics without any significant confinement effects. Hence, a smaller domain is chosen for the grid refined simulation.

The wall-normal grid resolution for DNS in rough-wall channel flows depends on k_{rms}^+ . Busse *et al.* (2015) recommended $\Delta y^+ < 1$ within the roughness layer and a maximum resolution of $\Delta y^+ \approx 5$ at the centerline of the channel for DNS. They used $\Delta y_{min}^+ = 0.667$ and $\Delta y_{max}^+ = 4.13$ for their rough turbulent channel simulations where $4.6 \leq k_{rms}^+ \leq 6.7$, implying $7 \sim 10$ cells within the roughness layer. For the present simulations, $k_{rms}^+ = 2.8$, hence the grid resolution is finer than that used by Busse *et al.* (2015) in the wall-normal

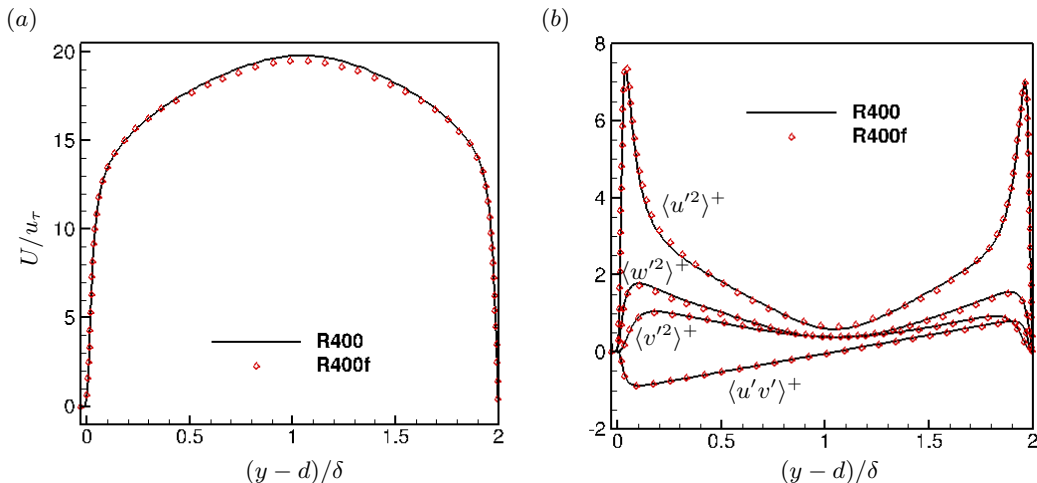


FIGURE 6. The grid-refined Case R400f compared to Case R400: (a) mean velocity profile and (b) Reynolds stresses in the outer coordinate.

direction. The streamwise and spanwise resolutions also adhere to the criteria suggested by Busse *et al.* (2015), shown in table 3.

Based on the resolution refinement, two original rough tiles are interpolated onto grids of size 667×200 . The interpolated tiles are then randomly rotated and tiled in the spanwise direction to achieve a domain size of $4\delta \times 2.4\delta$. The length, width and roughness heights of this generated rough surface are normalized by the channel half-height 12.5mm . The p.d.f. of the rough surface is demonstrated in figure 4(a), which shows good agreement with the p.d.f. of the original tiles. The mean velocity and Reynolds stresses profiles of Case R400f are compared to those of Case R400 in figure 6. Good agreement is observed in both profiles, meaning that Cases R400 and R600 are adequately resolved.

4. Results

4.1. Mean flow properties

4.1.1. Skin-friction coefficient

Since the top wall is smooth and the bottom wall is rough, the shear stress over the smooth wall, τ_w^t , is computed from the velocity field. The rough-wall shear stress τ_w^b is then computed from the force balance between the drag of the walls and the body force. The mean skin-friction coefficient $C_f = \tau_w^b / (0.5\rho U^2)$ is computed, where U is the streamwise mean velocity of the channel flow. Figure 7 shows C_f of the random-rough walls at the two Re_τ , along with the experimental results of Schultz & Flack (2013) for comparison. Note that the random-rough channel flow is hydraulically smooth at the low Reynolds number. The skin friction decreases as Re increases and the flow becomes transitionally rough. The viscous drag contributes to the overall skin friction in this flow regime. As Re further increases, the rough surface exhibits the fully-rough behaviour where the skin friction becomes independent of Re . The C_f values of Case R400 and Case R600 are shown in table 4. The errors of the simulation relative to experiment at the two Re_τ are 1.8% and 2.0%, which constitutes reasonable agreement.

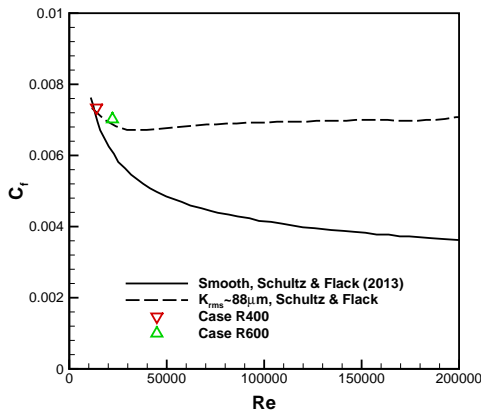


FIGURE 7. Skin-friction coefficient of Case R400 and Case R600, compared to the experimental results of the smooth and random-rough cases of Schultz and Flack.

Case	Experiment	DNS	Error
R400	0.00721	0.00734	1.8 %
R600	0.00688	0.00702	2.0 %

TABLE 4. Skin-friction coefficient from experiments and DNS for the random-rough cases.

4.1.2. Mean velocity profile

Mean velocity profiles of Case R400 and Case R600 are presented with different normalizations. Figure 8(a) shows the streamwise mean velocity profile in outer layer coordinates. U is normalized by the average friction velocity u_τ and y is shifted by subtracting the zero-plane displacement d (defined as the mean roughness height in rough cases), and then normalized by δ . The smooth cases at $Re_\tau = 395$ and $Re_\tau = 590$ from Moser *et al.* (1999) are also presented for comparison. A velocity deficit can be observed for the rough wall compared to the smooth cases. As expected, the decreased velocity is more significant in the lower half-channel. Compared to the smooth case, the peak of the mean velocity profile at $Re_\tau = 400$ decreases by 1.6% and shifts away from the rough wall by 5%. For a higher Re_τ , a more significant velocity deficit is observed. The peak mean velocity is reduced by 4.4% and shifted by 8.4% compared to the smooth case at the same Re_τ .

Figure 8(b) gives a closer view of the viscous wall region by showing the mean velocity in inner coordinates. The mean velocity and the wall-normal distance of the smooth cases are normalized by the average friction velocity u_τ and ν/u_τ respectively. The curves of the smooth wall at different Re_τ collapse in the inner coordinate. For the random-rough cases, the mean velocity is normalized by the bottom-wall friction velocity u_τ^b . This demonstrates the slip and drag effect of the rough walls more accurately as suggested by Alamé & Mahesh (2019). Since only the bottom wall is covered by the roughness, the maximum mean velocity in figure 8(a) is shifted towards the top wall and results in an asymmetric “half-length” δ_t for the upper half-channel and the lower half-channel. δ_t is defined by Bhaganagar *et al.* (2007), as an effective layer thickness for each side, which

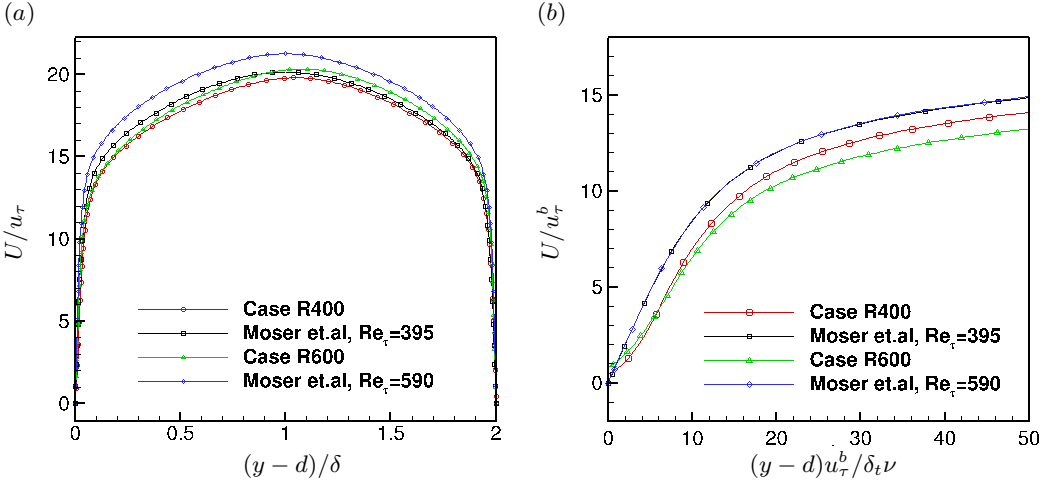


FIGURE 8. Mean velocity profile of Case R400 and Case R600 compared to the DNS of a smooth channel flow by Moser *et al.* (1999): (a) In the outer coordinate, where U is normalized by the average friction velocity u_τ as a function of the wall-normal distance y subtracted by the zero-plane displacement d and normalized by the channel half-height δ ; (b) In the near-wall region using the inner coordinate, where U is normalized by the bottom-wall friction velocity u_τ^b , $(y-d)$ is scaled by the effective layer thickness δ_t , normalized by u_τ^b/ν .

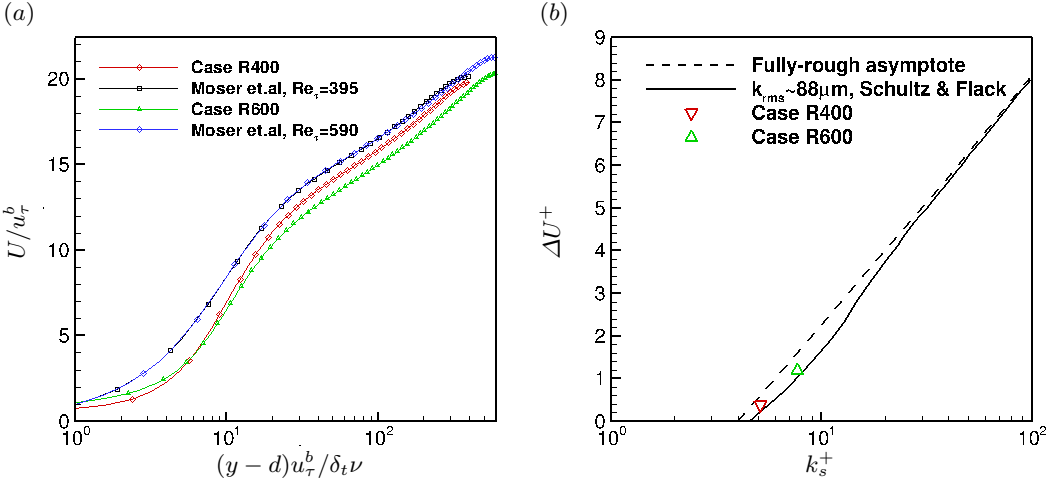


FIGURE 9. (a) Semi-log plot of the mean velocity profile in the inner coordinate and (b) the roughness function as a function of k_s^+ , compared to the experimental results from Schultz and Flack.

is evaluated by the distance from the virtual (or actual, for the smooth wall) origin to the location of the minimum velocity fluctuations (i.e. maximum mean velocity). The profile is then scaled by $\delta_t/\delta = 1.033$ and 1.055 , respectively, for the rough-wall side at $Re_\tau = 400$ and 600 . This scaling for the wall-normal location gives a better collapse of the logarithmic regions of the smooth and rough cases. Case R400 shows a slip velocity at the wall and the profile is lowered by 7.5% relative to the smooth case. The slip velocity is increased further for Case R600 and the profile is shifted downwards by 14.9%. The two profiles intersect at $y^+ = 5$. This indicates that a larger slip velocity exists at the wall and an overall increase of drag is exhibited in the viscous wall region as Re_τ increases.

The mean velocity profile is shown in figure 9(a) using the same scaling as figure 8(b), but in semi-log coordinate. Due to the slip effect of the roughness, the velocity profile shows a gradual increase away from the wall. This trend seems to end at $y^+ = 5$ which is the transition from the viscous sublayer to the buffer layer. In the buffer layer, Case R600 goes up more slowly and ends up with a more significant velocity deficit than Case R400. A similar trend was observed by Busse *et al.* (2017). In the log-law region, the smooth-wall profiles follow the logarithmic law:

$$U_s^+ = \frac{1}{\kappa} \ln y^+ + B, \quad (4.1)$$

where κ is the Von Karman constant and B is the intercept for a smooth wall. The rough-wall profiles conform to the log-law but display an offset from the smooth-wall profiles, where the roughness effect on mean velocity can be evaluated from this difference. Nikuradse (1933) found that the logarithmic velocity distribution for the mean velocity profile still held for rough walls, with the same value of κ as

$$U_r^+ = \frac{1}{\kappa} \ln(y/k_s) + 8.5 \quad (4.2)$$

The roughness function is obtained by taking the difference of mean velocities in wall units between smooth and rough walls within the logarithmic layer.

$$B - \Delta U^+ + \frac{1}{\kappa} \ln k_s^+ = 8.5 \quad (4.3)$$

A good collapse in the fully rough regime for different roughness types is found by Flack & Schultz (2010) when using k_s as the roughness scale. Since the shape of the roughness function in the transitionally rough regime differs with the roughness type and the onset of the fully rough regime is unknown for most surfaces, ΔU^+ with the corresponding roughness Reynolds number, k_s^+ , is presented in figure 9(b), and compared to the experimental results of Flack and Schultz. The results show that Case R400 and Case R600 are located in the transitionally rough regime, which is below the fully-rough asymptote, and match with the experimental results.

4.1.3. Reynolds stresses

The profiles of Reynolds stresses scaled by u_τ^2 in the outer coordinates are shown in figure 10. The roughness effect is most significant in the streamwise velocity fluctuations because the peak of $\langle u'u' \rangle$ is closer to the wall than the other components, as mentioned by Hu *et al.* (2006). The location of the peak of $\langle u'u' \rangle$ is Re_τ dependent, as shown in figure 10(a), both smooth and rough cases at $Re_\tau = 600$ is closer to the wall than cases at $Re_\tau = 400$. The peak of $\langle u'u' \rangle$ in the lower half-channel at $Re_\tau = 400$ is decreased by 2.8% compared to the smooth case of Moser *et al.* (1999). This is consistent with Busse *et al.* (2015). The roughness causes the reduction of the streamwise velocity fluctuations at the peak. The outer part of the profile has a better agreement with the smooth case. However, the valley of the profile is shifted to the top wall by 7.9% due to the existence of roughness. For the upper half of the channel, from $y/\delta = 1$ to 2, the profile is shifted downwards from the smooth case. For $Re_\tau = 600$, the peak value of $\langle u'u' \rangle$ is further decreased by 9.1% and the valley of the profile is shifted to the top wall by 9.2%. The peak of $\langle u'u' \rangle$ is even lower with a higher Re_τ which indicates that the roughness effect becomes more significant on the streamwise velocity fluctuations as Re_τ increases.

The roughness effect on the wall-normal Reynolds stress is presented in figure 10(b). Compared to Moser *et al.* (1999)'s smooth cases, unlike the streamwise velocity fluctuations, the bottom part of $\langle v'v' \rangle$ profile is increased, while the top part of $\langle v'v' \rangle$

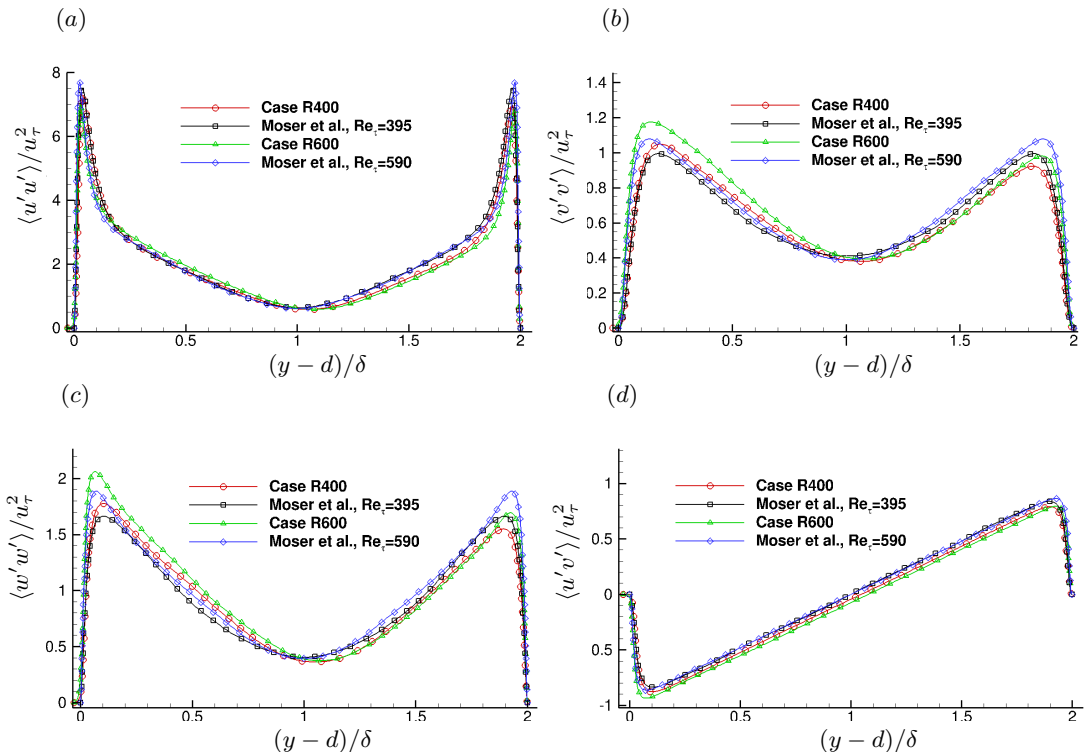


FIGURE 10. Velocity fluctuations in the outer coordinate: (a) streamwise, (b) wall-normal, (c) spanwise components, and (d) Reynolds shear stress.

is decreased. The peak value of $\langle v'v' \rangle$ is increased by 5.3% at $Re_\tau = 400$ and 8.9% at $Re_\tau = 600$. As Re_τ increases, the velocity fluctuations for random-rough cases are increased. The bottom part of the profile shows an even stronger enhancement.

The level of spanwise velocity fluctuations is increased by the roughness, shown in the bottom part of profile in figure 10(c). The profile is shifted at the same rate as the streamwise and wall-normal velocity fluctuations, and shows a decrease in the top part compared to the smooth cases. The peak value of $\langle w'w' \rangle$ in the bottom part has a more prominent amplification than the peak values in the top part as Re_τ increases.

The profile of Reynolds shear stress is decreased by the roughness, as shown in figure 10(d). This disagrees with the observation by Busse *et al.* (2015) that the peak of $\langle u'v' \rangle$ is increased. They also found that the outer part of the profile has an agreement with the smooth-wall case. However, our results show an obvious higher level for the bottom part and a lower level for the top part for $\langle u'u' \rangle$, $\langle v'v' \rangle$ and $\langle w'w' \rangle$, and a downward shift for the whole profile of $\langle u'v' \rangle$. This is because the channel flow simulation by Busse *et al.* (2015) were roughened for both top and bottom walls, while our simulation is only bottom-wall roughened, where the profile is asymmetric and shifted by the existence of roughness. The friction velocity is different due to this asymmetry of the wall conditions, which indicates that different scalings for the upper half and lower half of the profile need to be considered.

To investigate an appropriate scaling for Reynolds stresses, the top and bottom part of the profile are plotted separately in the inner coordinate. Figure 11(a) shows the Reynolds stresses scaled by the average friction velocity u_τ at $Re_\tau = 400$ compared to the smooth channel flow of Moser *et al.* (1999). The streamwise and spanwise velocity

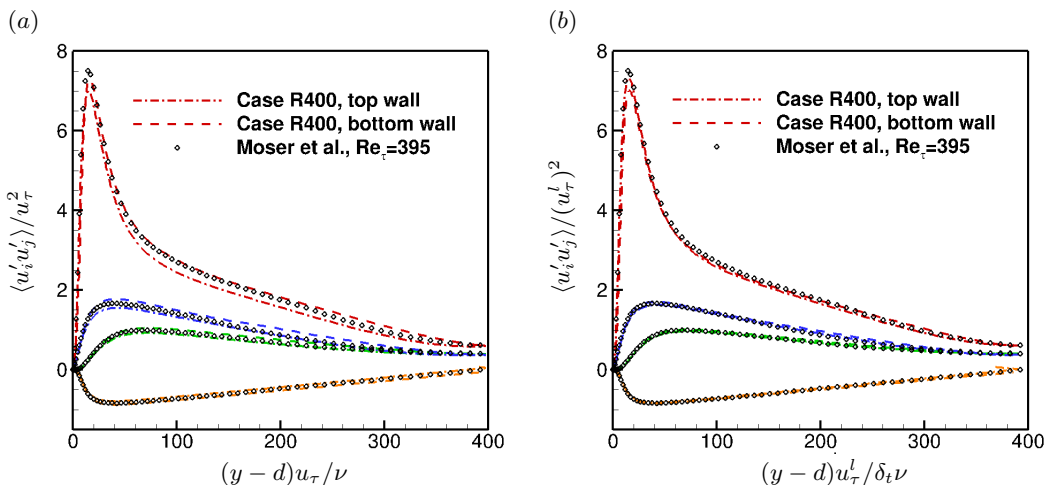


FIGURE 11. DNS of a random-rough channel flow at $Re_\tau = 400$ compared to the DNS of Moser *et al.* (1999): (a) Reynolds stresses scaled by average friction velocity u_τ^2 in inner-layer units and (b) Reynolds stresses scaled by local friction velocity $(u_\tau^l)^2$ in the inner coordinate normalized by δ_t .

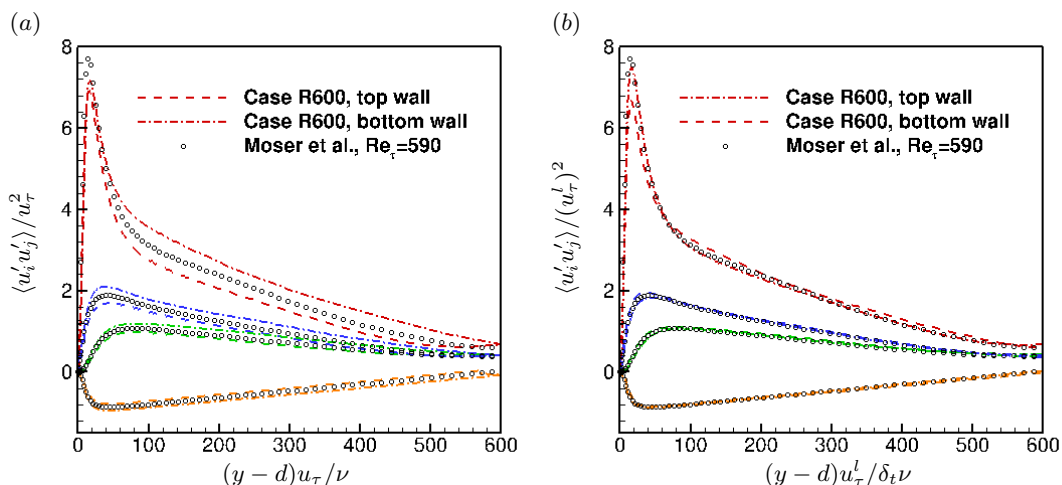


FIGURE 12. DNS of a random-rough channel flow at $Re_\tau = 600$ compared to the DNS of Moser *et al.* (1999): (a) Reynolds stresses scaled by average friction velocity u_τ^2 in inner-layer units and (b) Reynolds stresses scaled by local friction velocity $(u_\tau^l)^2$ in the inner coordinate normalized by δ_t .

fluctuations demonstrate a higher level than the wall-normal direction. Both the smooth and rough-wall sides have a decreased peak value of $\langle u'u' \rangle$, but the rough-wall side is further decreased due to the existence of roughness. The outer part of $\langle u'u' \rangle$ shows a slight deviation from the smooth case. The wall-normal, spanwise fluctuations and Reynolds shear stress for the rough-wall side have a higher level while those of the smooth-wall side present a lower level. Figure 11(b) demonstrates a different scaling, the Reynolds stresses are scaled by the local friction velocity u_τ^t for the smooth-wall side, and u_τ^b for the rough-wall side. The effective layer thickness δ_t ($\delta_t/\delta = 1.033$ and 0.967 , for the rough-wall side and the smooth-wall side respectively) is used to normalize the profiles. The result shows better agreement. The peak value of $\langle u'u' \rangle$ presents the most significant difference

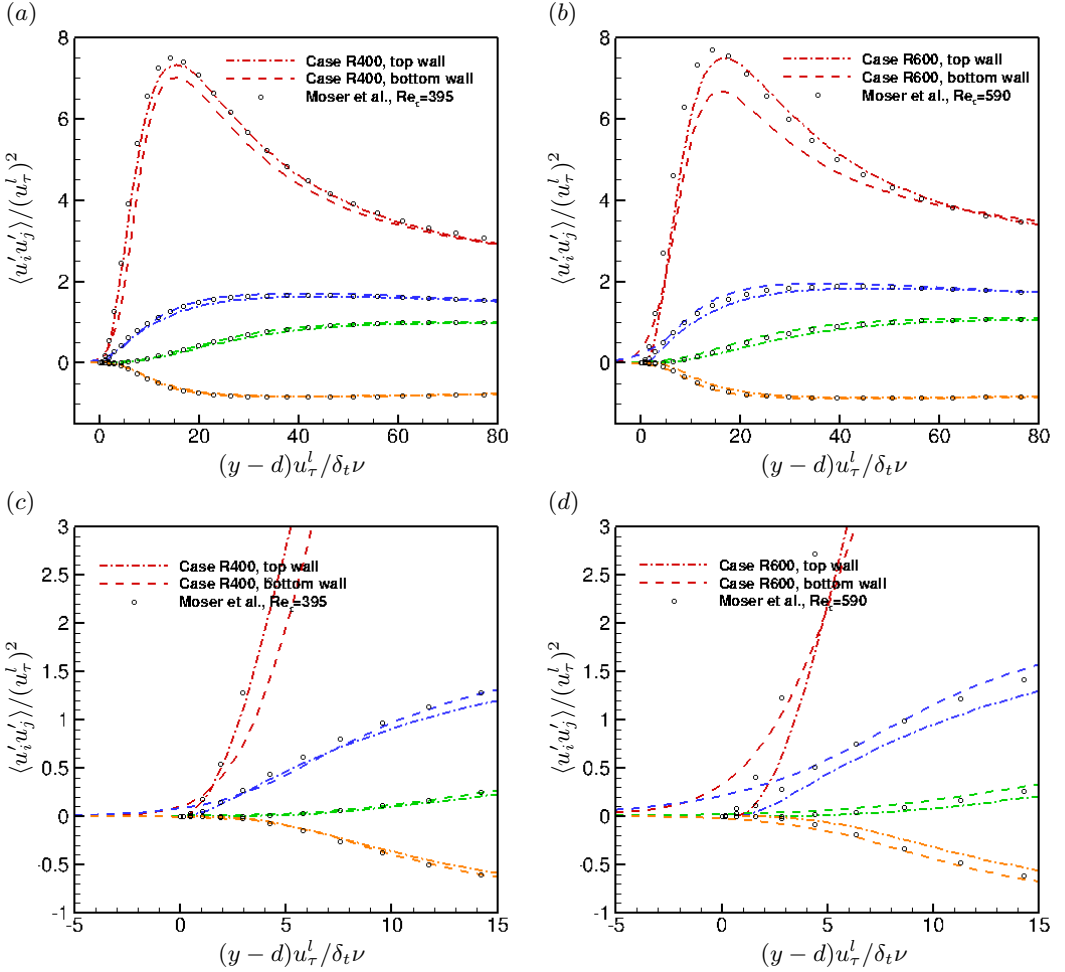


FIGURE 13. Zoom-in views in the near-wall region: (a) Case R400 and (b) Case R600; Zoom-in views in the roughness layer: (c) Case R400 and (d) Case R600.

compared to other components. The rough-wall side has a decreased peak value while the smooth-wall side matches well with the smooth case. For $Re_\tau = 600$, the different scalings are compared in figure 12. Figure 12(a) shows a more significant difference between the smooth-wall side and the rough-wall side when normalized by the average friction velocity, meaning that the velocity fluctuations are enhanced as Re_τ increases. However, when the profile is scaled by the local friction velocity and the effective layer thickness, a better collapse in the outer part of the profile is obtained, shown in figure 12(b). For the streamwise velocity fluctuations, the profile of the smooth-wall side matches with Moser *et al.* (1999)'s smooth case, while the outer part of the rough-wall profile agrees with the smooth case but the peak value presents a larger decrease than that of Case R400. The results suggest that it is necessary to normalize the profiles by the local friction velocity and the effective layer thickness. The roughness effects on Reynolds stresses are limited to the near-wall region and the outer-layer similarity is maintained.

Close-up views of the near-wall region are shown in figure 13. An overall increase in the level of velocity fluctuations is observed at higher Re_τ . A similar observation for smooth channel flows with increasing Re_τ was made by Hu *et al.* (2006). The streamwise

component of the rough-wall side shows a significant reduction near the peak location, and an increase around $y = 0$. This is consistent with the general observations for rough surfaces. The spanwise component shows an increased level at the peak and in the roughness layer, which is in agreement with the observations by Busse *et al.* (2015). For the wall-normal component, a relatively weaker enhancement is shown at the peak of $\langle v'v' \rangle$ as well as the region close to $y = 0$. Busse *et al.* (2015) found that an increase occurs at the peak of the wall-normal Reynolds stress only for the surface with the highest level of filtering, which corresponds to the surface with the smallest roughness height ($k_{rms}^+ = 4.6$) and the largest skewness ($sk = 1.15$). For other cases, the peak value is decreased with the decreasing level of filtering. In the roughness layer, they found that the wall-normal Reynolds stress is increased at the wall with a decreasing amount of filtering, and the higher wall-normal velocity fluctuations occur upstream of larger roughness elements. An increase of the wall-normal velocity fluctuations within the roughness layer and a decrease above the roughness layer for high roughness are also observed from the data of De Marchis *et al.* (2010). These suggest that the wall-normal velocity fluctuations could depend on the scale and variation of the roughness elements. Since the roughness statistics of Case R400 and Case R600 are quite different from that of Busse *et al.* (2015), where the roughness height in wall units of Case R400 and Case R600 is smaller than theirs, a less significant increase at the wall and a slight increase at the peak for the wall-normal velocity fluctuations can be expected. The Reynolds shear stress after the normalization does not show as much difference as other components. Busse *et al.* (2015) found that the Reynolds shear stress is decreased with an increasing roughness height. Case R400 and Case R600 does not show such an obvious decrease. This could be explained from the mean momentum equation. The total shear stress in the smooth channel flows can be derived from the streamwise mean momentum equation, expressed in the form as: $\tau = \rho\nu\frac{d\langle U \rangle}{dy} - \rho\langle uv \rangle$ (Pope 2001). If τ is normalized by the average friction velocity u_τ , the shear stress of the smooth-wall flows can be written as:

$$\frac{\tau}{\rho u_\tau^2} = \frac{1}{u_\tau^2} \left(\nu \frac{d\langle U \rangle}{dy} - \langle uv \rangle \right) \quad (4.4)$$

In the rough-wall cases, since the velocity field is not homogeneous in the near-wall region, the total shear stress would be modified by adding an inhomogeneous term and normalized by the rough-wall friction velocity u_τ^b :

$$\frac{\tau}{\rho (u_\tau^b)^2} = \frac{1}{(u_\tau^b)^2} \left(\nu \frac{d\langle U \rangle}{dy} - \langle uv \rangle - \frac{1}{\rho} \int \left(\frac{\partial \langle uu \rangle}{\partial x} + \frac{\partial \langle uw \rangle}{\partial z} \right) dy \right) \quad (4.5)$$

These three terms on the right-hand side have to balance each other. As shown in figure 8(b), the first term $\rho\nu\frac{d\langle U \rangle}{dy}$ is decreased in the random-rough cases at the same wall-normal location compared to the smooth cases. To maintain the balance, the summation of the other terms has to be increased. When the flow is more inhomogeneous, the term $\int \left(\frac{\partial \langle uu \rangle}{\partial x} + \frac{\partial \langle uw \rangle}{\partial z} \right) dy$ becomes larger, resulting in the fact that the absolute value of the Reynolds shear stress has to be decreased compared to smooth cases. Since the present rough surface has a smaller scale, which does not induce flow inhomogeneity as strong as higher roughness, a slight decrease of Reynolds shear stress in the near-wall region is observed in Case R400 and Case R600.

4.1.4. Mean-square pressure fluctuation

The mean-square pressure fluctuations $\langle p'^2 \rangle^+$ are investigated in the outer and inner regions at the two Re_τ . Figure 14(a) shows the mean-square pressure in the outer variable y/δ for Case R400 and Case R600, compared to the results of Case SW and the smooth

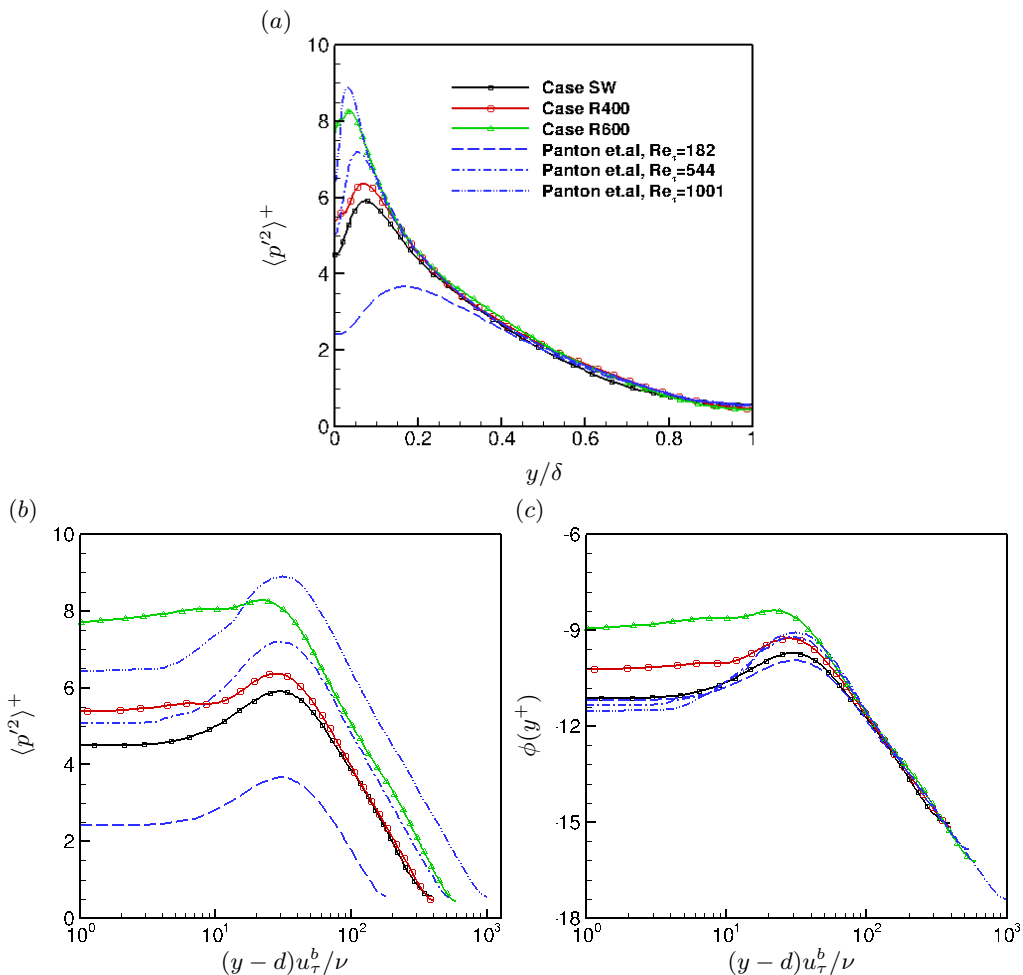


FIGURE 14. Pressure fluctuation profiles (a) in the outer coordinate, (b) in the inner coordinate and (c) inner correlation function $\phi(y^+)$.

channel flows by Panton *et al.* (2017) for various Re_τ . As the wall-normal location moves away from the wall, $\langle p'^2 \rangle^+$ increases and reaches the peak, then decreases and all curves including smooth and rough cases collapse quite well, following the logarithmic matching law fitted by Panton *et al.* (2017),

$$\langle p'^2 \rangle_{cp}^+(y/\delta) = -2.5625 \ln(y/\delta) + 0.2703 \quad (4.6)$$

As Re_τ increases, the level of $\langle p'^2 \rangle^+$ shows an overall increase before decreasing into the logarithmic matching law and the peak location moves closer to the wall. For the random-rough cases, $\langle p'^2 \rangle^+$ shows a higher level before the collapse of the logarithmic matching law. The mean-square pressure in the inner coordinate is shown in figure 14(b). An overall increased level is observed as Re_τ increases. The profiles maintain constant values in the viscous sublayer, then show a gradual rise as the wall-normal location moves away from the wall. They reach the peak at $y^+ = 30$, and finally drop off in a logarithmic decline. Comparing Case R400 to Case SW, the level of pressure fluctuations is significantly increased by 20.2% within the roughness layer. In the region above the roughness layer, the pressure fluctuation is enhanced by 7.8%. After reaching

the peak, the enhancement gradually disappears and the profiles of Case SW and Case R400 collapse in the logarithmic decline, suggesting that the roughness effect on pressure fluctuations disappears in the outer layer. For Case R600, the enhancement of pressure fluctuations in the roughness layer is even stronger and almost reaches the level of the peak value. To eliminate Re_τ dependence, an inner correlation function was derived by Panton *et al.* (2017),

$$\phi(y^+) = \langle p'^2 \rangle^+(y^+, Re_\tau) + 2.5625 \ln(Re_\tau) - 0.2703 \quad (4.7)$$

The inner correlation function shows a good correlation beyond $y^+ = 50$ in figure 14(c). The increased level of pressure fluctuations below $y^+ = 50$ can be evaluated from the difference between the smooth and random-rough cases. It can be concluded that the roughness has increased pressure fluctuations in the inner layer and the enhancement is much stronger for higher Re_τ .

4.1.5. Mean momentum balance

The mean momentum balance (MMB) for the rough-wall turbulent channel flows reveals the contribution of the various terms in the governing equation, and the mean roughness effect on the dynamical mechanisms. Mehdi *et al.* (2010) investigated the layer structure associated with MMB using rough-wall experimental data sets and found that the results are quite scattered due to the difficulty to obtain high quality Reynolds stress data from experiments. They obtained a better collapse for the viscous to Reynolds stress gradient ratios by using the normalized distance from the peak Reynolds stress location. The MMB is examined below for our rough-wall channel flow simulations.

The roughness elements are three-dimensional and irregular so that they distort the streamwise mean flow in the near-wall region. The streamwise mean momentum equation for a fully-developed channel flow is

$$\frac{\partial \langle U \rangle}{\partial t} + \underbrace{\frac{\partial \langle U \rangle \langle U_j \rangle}{\partial x_j}}_A = - \underbrace{\frac{1}{\rho} \frac{\partial \langle P \rangle}{\partial x}}_B + \underbrace{\nu \frac{\partial^2 \langle U \rangle}{\partial x_j^2}}_C - \underbrace{\frac{\partial \rho \langle u' u'_j \rangle}{\partial x_j}}_D + \langle K \rangle, \quad (4.8)$$

where the subscript j denotes streamwise, wall-normal and spanwise components for velocity and position vectors and K is the imposed body force. In this equation, term A accounts for mean advection, term B represents the form drag (pressure gradient), term C shows the viscous force (viscous stress gradient) and term D is the net effect of turbulent inertia (Reynolds stress gradient). The mean advection is zero in the turbulent channel flow. Figure 15(a) shows the contribution of term B, C and D to the mean momentum equation against y^+ , while figure 15(b) presents the ratio of the viscous stress gradient to the Reynolds stress gradient.

Case SW is firstly examined and the properties of its MMB layer structure are compared to Wei *et al.* (2005). Since the wall is smooth, the mean advection and pressure gradient is zero. The viscous stress gradient, Reynolds stress gradient and the body force must be in balance. As y^+ goes to zero, the Reynolds stress is zero and the balance is between the viscous stress gradient and the body force. The magnitude of the ratio therefore becomes increasingly large in the viscous sublayer (layer 1). As y^+ increases from 5 to 30, corresponding to the buffer layer (layer 2), the viscous and Reynolds stress gradient have the similar variation and reach the peak value at $y^+ = 7.8$. The magnitude of the ratio is therefore close to unity. As y^+ further increases from 30 to 60 (layer 3), the viscous term decreases to zero. The Reynolds stress gradient decreases at the same rate but finally maintains its magnitude to balance the body force. In this layer, the Reynolds

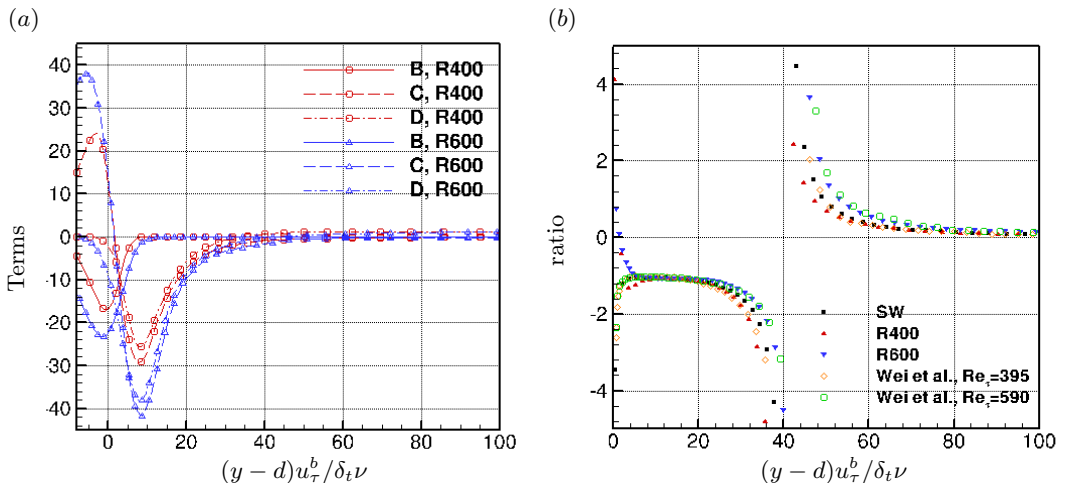


FIGURE 15. (a) Contribution of terms to the mean momentum equation against y^+ ; (b) The MMB layer structure for Case R400 and R600 compared to smooth cases, shown by the ratio of the viscous to the Reynolds stress gradients.

stress gradient changes from negative to positive values at $y^+ = 40$, corresponding to the peak Reynolds stress location. When y^+ goes above 60 (layer 4), the viscous effect disappears and the balance is between the body force and the Reynolds stress gradient.

The results of the random-rough cases are also shown in figure 15. Case R400 is examined and compared to Case SW at $Re_\tau = 400$ in figure 15(a). The viscous stress gradient is enhanced in the valley region (below the mean height location, i.e., $y^+ < 0$). As y^+ increases, it reaches a maximum value at $y^+ = -3$ and then decreases to negative values and has a similar variation as the smooth case. The peak occurs at the same location $y^+ = 7.8$ as Case SW with an increased magnitude, and agrees with Case SW above $y^+ = 15$, which approximately corresponds to the outer region above the roughness elements. The Reynolds stress gradient is increased near the mean height location $y^+ = 0$, which is consistent with the fact that the velocity fluctuations are enhanced due to the roughness. Then the Reynolds stress gradient follows similar variation as Case SW, has a higher peak value, and passes through zero before $y^+ = 40$. Moving further away from the wall, it finally collapses with Case SW, and balances the body force. The pressure gradient in the streamwise direction for rough cases is also plotted against y^+ . Term B is zero in Case SW as expected, however, is non-zero in Case R400 because the roughness elements cause the form drag. As y^+ increases, the pressure gradient increases to achieve a negative peak value at the mean height location, and reduces to zero when y^+ reaches the edge of the rough region.

Figure 15(b) shows the ratio of the viscous stress gradient to the Reynolds stress gradient for both smooth and rough cases. In the rough region, since the pressure gradient and viscous stress gradient are produced and enhanced by the roughness, the MMB layer structure is different from the smooth cases. As y^+ approaches zero, the ratio goes to an increasingly positive value, due to the enhanced positive value of the viscous term. In the buffer layer, the profile of Case R400 has a good agreement with the smooth cases. The stress gradient balance is maintained between the viscous and Reynolds stress gradients since the pressure gradient does not affect the mean flow above the rough region. In layer 3, the transition location where the ratio changes sign is closer to the rough wall compared to the smooth cases at the same Re_τ . This is consistent with Wei *et al.* (2005),

they suggest that the roughness induces a more rapid three-dimensionalization of the vorticity field in the near-wall region, causing the logarithmic-like behaviour occur closer to the wall. This influence of roughness on the MMB layer structure is more clearly to be observed in the simulations. In layer 4, the ratio for Case R400 agrees well with the smooth cases and approaches zero as the viscous effect becomes weak.

The Re_τ effect on the MMB is also investigated in figure 15(a). The viscous stress gradient of Case R600 has a higher magnitude than Case R400 in the valley region, and decreases to zero at the same location $y^+ = 1.7$, corresponding to the maximum value of the viscous stress. The pressure gradient and Reynolds stress gradient are increased within the rough region. In the buffer layer, both the viscous and Reynolds stress gradients are enhanced tremendously at higher Re_τ . As y^+ further increases above 30, the roughness effect and Re_τ dependence are weakened, the viscous stress gradient reduces to zero and the Reynolds stress gradient balances the body force. In figure 15(b), the ratio of viscous to Reynolds stress gradients for Case R600 shows similar features in layer 1 as Case R400. However, the thickness of layer 2 is larger and the transition shifts further away from the wall to $y^+ = 44$ at higher Re_τ . The transition for Case R600 occurs closer to the wall than the smooth case by Wei *et al.* (2005). The results suggest that the roughness effect is mainly imposed on the rough region, and is damped out as y^+ increases above the buffer layer. The rough-wall flow in general maintains the similar features of the MMB layer structure, but modifies layer 1 due to the enhanced viscous stress gradient, as well as moving the transition location in layer 3 closer to the wall.

4.2. Statistics of wall-shear stress fluctuations

The statistics of wall-shear stress fluctuations are examined in this section. Case SW is the baseline, whose statistics of wall shear-stress fluctuations show good agreement with the results of a smooth-wall turbulent boundary layer of Diaz-Daniel *et al.* (2017). The rod-roughened channel (Case RRW) is also examined to establish both equivalence and contrast with the random rough walls. Case RRW is divided into two separate regions and wall-shear stress signals on projected surfaces are examined. One region is the top surface of the rod, the other is the bottom surface within the cavity between the rods. Similarly, for Case R400 and Case R600, the signals are probed separately in two regions. The mean height location of the roughness is chosen to be the reference plane, and the rough surface is divided into the peak regions, above the mean height location, and the valley regions, below the mean height location. The statistics of wall-shear stress signals are expected to perform differently with various surface topographies, which suggests decomposing the surface and investigating the correlation between the wall-shear stress fluctuations and the roughness geometries. A schematic of the decomposition is shown in figure 16. The wall-shear stress components on the projected surface are defined as

$$\tau_{yx} = \rho\nu\left(\frac{\partial u(t)}{\partial y} + \frac{\partial v(t)}{\partial x}\right) \quad (4.9)$$

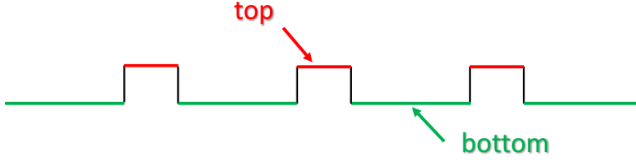
$$\tau_{yz} = \rho\nu\left(\frac{\partial w(t)}{\partial y} + \frac{\partial v(t)}{\partial z}\right) \quad (4.10)$$

The wall-shear stress fluctuations are denoted by τ'_{yx} and τ'_{yz} , and the rms values are expressed as $\tau_{yx,rms}$ and $\tau_{yz,rms}$.

4.2.1. p.d.f. of wall-shear stress

The p.d.f. of the streamwise shear stress component τ_{yx} , spanwise shear stress component τ_{yz} , and the shear-stress yaw angle $\phi_\tau = \tan^{-1}(\tau_{yz}(t)/\tau_{yx}(t))$ is investigated for the

Rod-roughened wall:



Random-rough wall:

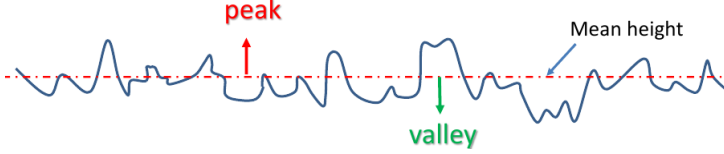


FIGURE 16. Sketch of data probe for rough-wall shear stress fluctuations

Case	region	Re_τ	$\mu(\tau_{yx})$	$\sigma(\tau_{yx})$	$Sk(\tau'_{yx})$	$Ku(\tau'_{yx})$	$\mu(\tau_{yz})$	$\sigma(\tau_{yz})$	$Sk(\tau'_{yz})$	$Ku(\tau'_{yz})$	$\sigma(\phi_\tau)$
SW	-	400	1.09	0.40	0.97	4.50	1.45e-2	0.25	-0.18	8.79	14.54
RRW	top	400	1.89	1.52	1.79	7.30	-3.48e-3	0.78	5.77e-2	8.72	25.01
RRW	bottom	400	-0.27	0.32	-2.03	11.56	-2.10e-3	0.35	2.45e-2	10.86	138.07
R400	peak	400	1.34	1.25	2.21	11.00	3.95e-3	0.54	-1.28e-2	10.09	32.52
R400	valley	400	0.21	0.37	2.22	13.09	-7.11e-3	0.29	-0.17	14.72	80.65
R600	peak	600	1.42	1.43	2.08	9.85	-7.23e-4	0.71	-1.82e-2	11.48	41.94
R600	valley	600	0.20	0.50	2.49	16.66	-1.42e-2	0.40	-0.40	19.47	93.78

TABLE 5. Statistics of the wall-shear stress components τ_{yx} , τ_{yz} and yaw angle ϕ_τ : mean $\mu(\cdot)$, standard deviation $\sigma(\cdot)$, skewness $Sk(\cdot)$, kurtosis $Ku(\cdot)$ for smooth, rod-roughened and random-rough channel flow at $Re_\tau = 400$ and $Re_\tau = 600$.

rod-roughened and random-rough channel flows at two Re_τ . The results are compared in figure 17 -19. The statistical properties of these variables are shown in table 5.

The rms fluctuations of the streamwise shear stress for Case SW, shown in table 5, are in good agreement with the correlation $\tau_{yx,rms}^+ = \tau_{yx,rms}/\tau_w = 0.298 + 0.018 \ln Re_\tau$, proposed by Örlü & Schlatter (2011). However, this correlation is not valid for rough-wall channel flows since the definition of τ_w is no longer simply expressed by the mean value of τ_{yx} . Compared to Case SW at the same Re_τ , an obvious increase in $\tau_{yx,rms}$ is seen for the top surface of Case RRW and the peak region of Case R400, while a slight decrease is seen for the bottom surface of Case RRW as well as the valley region of Case R400. This implies that the signals of τ_{yx} have a higher level of fluctuations on the top surface of the rods, and in the peak region of the random-rough surface. Similar features are also demonstrated in figure 17(a), a significant increase in the probability of events with positive τ_{yx} can be observed for the top surface of Case RRW and the peak region of the random roughness. The streamwise wall-shear stress with large positive values is mainly contributed by the large streamwise velocity gradient in the wall-normal direction. This is because that the streamwise velocity increases as y^+ goes further away from the wall

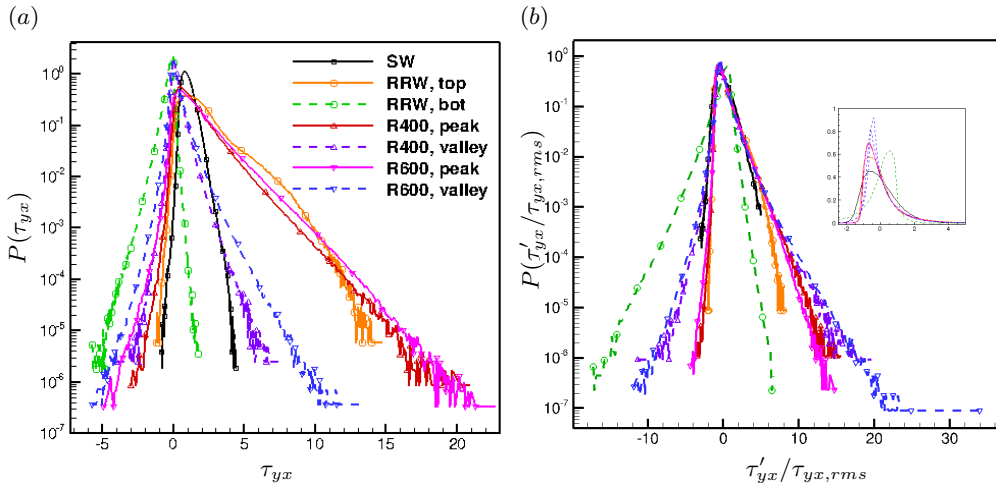


FIGURE 17. (a) Probability distribution function (p.d.f.) of the streamwise wall-shear stress on a semi-log scale and (b) p.d.f. of the streamwise wall-shear stress fluctuations on a semi-log scale, non-dimensionalized using the rms values, for Case SW, RRW, R400 and R600. The inset in (b) is shown on a normal scale.

in the peak region ($y^+ > 0$). The results are consistent with the observation that the streamwise mean velocity and velocity fluctuations are enhanced near $y^+ = 0$ in §4.1.

Case SW shows that the p.d.f. profile of τ_{yx} has a positive skewness and partly follows a log-normal distribution. Compared to Case SW, shown in table 5, the skewness of all rough cases has an increased magnitude, which results from the enhanced fluctuations by the roughness elements. Only the bottom surface of Case RRW is negatively skewed, which means that the streamwise wall-shear stress fluctuations are negatively dominant. This is due to the fact that two recirculating zones fill up most of the cavity region, as shown in figure 20(a). A large separation is formed downstream of the rod, whereas a smaller vortex is located upstream of the adjacent rod. For the random-rough case, the probability of events with negative τ_{yx} is increased compared to Case SW. The valley region shows a higher probability than the peak region. This reveals that the back flow occurs more frequently in the valley region than in the peak region. This is consistent with Lenaers *et al.* (2012) that the reverse flow occurs predominantly in low-speed streaks which are usually located close to the wall. Figure 20(b) demonstrates the near-wall streamline pattern for Case R400. The vortices are mainly located in the valley of the roughness, but are not as strong as the circulation between two adjacent rods.

The kurtosis of Case SW $Ku = 4.50$ is larger than $Ku = 3$ for a normal Gaussian distribution. The kurtosis is generally increased in the rough cases, meaning that the probability of the extreme events is increased by the roughness. The random-rough cases have an even higher kurtosis than the rod-roughened case, suggesting that the random-rough elements cause the extreme events to occur more frequently. The same feature can be observed in figure 17(a), where the p.d.f. of the peak region in Case R400 has a similar distribution as the p.d.f. of the top surface in Case RRW, however, the tails of the random-rough p.d.f. are wider. Diaz-Daniel *et al.* (2017) suggested that the probability of extreme events becomes higher with increasing Re for smooth-wall turbulent boundary layers. Figure 17(a) shows that, in general, the p.d.f. of Case R600 shows a similar distribution as the p.d.f. of Case R400, but the distribution tail at higher Re_τ is wider, especially the positive tail of the valley region, meaning that the probability of extreme events is larger at higher Re_τ . However, the results show that the Re_τ effect on the p.d.f.

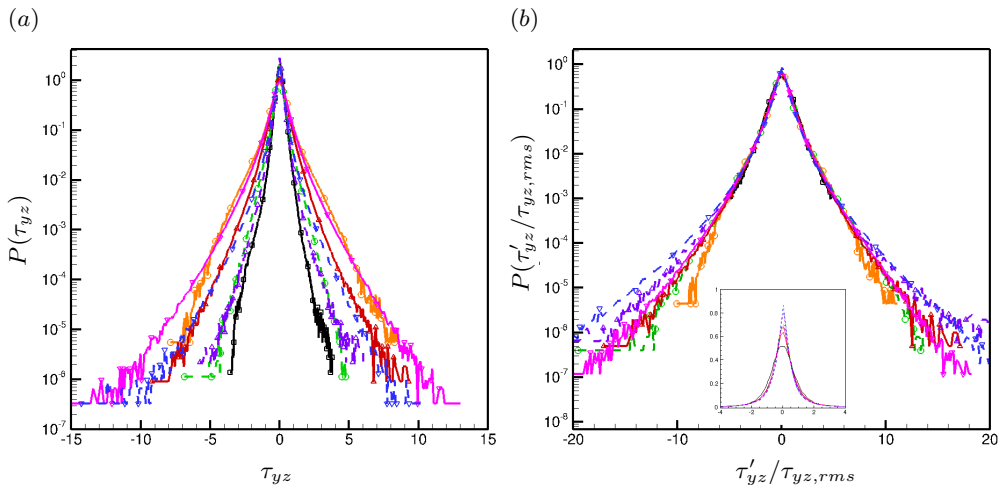


FIGURE 18. (a) Probability distribution function (p.d.f.) of the spanwise wall-shear stress on a semi-log scale and (b) p.d.f. of the spanwise wall-shear stress fluctuations on a semi-log scale, non-dimensionalized using the rms values, for Case SW, RRW, R400 and R600. The inset in (b) is shown on a normal scale.

profile is much less significant for this low range of Re_τ than the roughness effect. After the p.d.f. is normalized by subtracting the mean and dividing by the rms value, shown in figure 17(b), both Re_τ dependence and roughness effect are eliminated to some extent, and the p.d.f. has a better collapse. The kurtosis of the valley region for the random-rough cases is larger than that of the peak region, which corresponds to the wider tails of the p.d.f. for the valley region than the peak region.

The p.d.f. of spanwise wall-shear stress fluctuations τ_{yz} , shown in figure 18(a), has zero mean and zero skewness for smooth, rod-roughened, and random-rough cases. The rms of τ_{yz} has a higher value over the top surface of the rods and the peak regions of the random roughness, than the bottom surface and the valley regions. This is attributed to the increased velocity magnitude at higher wall-normal distance. As Re_τ increases, the fluctuations of τ_{yz} are enhanced. The tail of the p.d.f. of Case R600 is widened, suggesting the probability of extreme events increases. After normalizing by the mean and rms values, the p.d.f. profile has a better collapse, especially near the peak of the p.d.f., as shown in figure 18(b). However, the tail of the p.d.f. is Re_τ dependent. Higher Re_τ shows an increased probability at the tail of the p.d.f. distribution. The tail is also related to the location in the roughness. The bottom surface of the rod-roughened wall and the valley region of the random-rough wall have larger kurtosis than the top surface and the peak region after normalization.

The probability distribution of the shear-stress yaw angle $\phi_\tau(t) = \tan^{-1}(\tau_{yz}(t)/\tau_{yx}(t))$ is shown in figure 19. Jeon *et al.* (1999) found that the probability for events with $|\phi_\tau| > 45^\circ$ is very small in smooth channel flows. This means that the large, positive τ_{yx} are associated with relatively small τ_{yz} . Compared to Case SW, the standard deviation of ϕ_τ is much higher in the rough cases. The probability of events with $45^\circ < |\phi_\tau| < 90^\circ$ is enhanced by the roughness, indicating that the events with the relatively small τ_{yx} related to larger τ_{yz} have an increased probability. These results are consistent with the finding in the instantaneous streamwise velocity field (figure 25), where the streaks are observed to be broken up by the roughness elements, resulting in the larger probability of the events with smaller τ_{yx} . The p.d.f. profiles of the top surface and the peak region have a very different distribution compared to the p.d.f. of the bottom surface and the

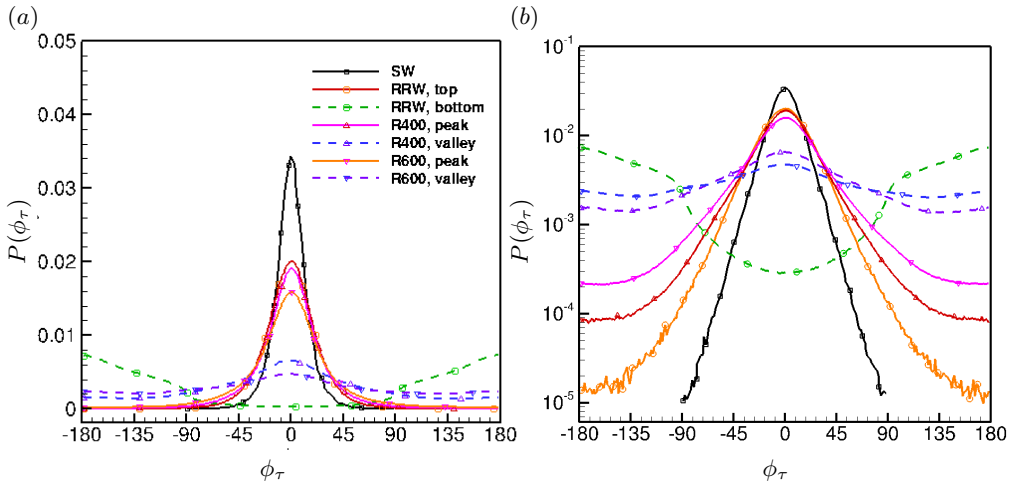


FIGURE 19. p.d.f. of the angle formed between the shear-stress vector and the streamwise direction for Case SW, RRW, R400 and R600: (a) in the normal coordinate and (b) in the semi-log coordinate.

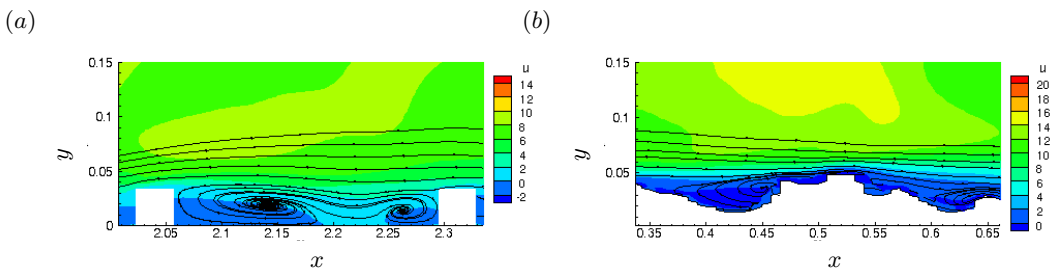


FIGURE 20. Streamwise velocity fields and streamline pattern in the vicinity of the roughness elements: (a) Case RRW and (b) Case R400.

valley region, shown in figure 19(a). First, the top surface in Case RRW and the peak region in random-rough cases are investigated. At $Re_\tau = 400$, the top surface in Case RRW and the peak region in Case R400 have a similar shape. Both of them have a drop in probability for the events with $0^\circ < |\phi_\tau| < 15^\circ$, but have an increased probability for the events with $|\phi_\tau| > 15^\circ$. For the events with $|\phi_\tau| > 45^\circ$, a higher probability in Case R400 compared to Case RRW is clearly demonstrated by the semi-log profile of the p.d.f. in figure 19(b), meaning that the random roughness increases the probability of the events with large and negative τ_{yx} associating with the smaller τ_{yz} . The probability of the events with large yaw angle becomes higher in Case R600, which suggests that higher Re_τ for rough cases enhances the probability of the events with large and negative τ_{yx} associating with the smaller τ_{yz} .

Now, we consider the bottom surface in Case RRW and the valley region in random-rough cases. Unlike the similarity in p.d.f. profiles between the top surface of Case RRW and the peak region of Case R400 and Case R600, the p.d.f. of the bottom surface and the valley region show some differences. The p.d.f. of the bottom surface and the valley region is more evenly distributed compared to Case SW. One significant difference is that the events with $90^\circ < |\phi_\tau| < 180^\circ$ have a much higher probability for the bottom surface in Case RRW while they have an almost zero probability for the events with $0^\circ < |\phi_\tau| < 45^\circ$. The high probability for the events with $90^\circ < |\phi_\tau| < 180^\circ$ implies that on the bottom surface τ_{yx} is mainly negative, which is attributed to that the

flow features are strongly dominated by the recirculation zones in the cavity. For the random-rough cases, the p.d.f. has a decreased value for the events with $0^\circ < |\phi_\tau| < 45^\circ$, but an increased value for the events with $|\phi_\tau| > 45^\circ$, compared to the p.d.f. of the peak region. This means that compared to the peak region, the events for large and positive τ_{yx} associating with relatively smaller τ_{yz} occur less frequently, while the events for small and positive τ_{yx} associating with relatively larger τ_{yz} occur more frequently. The presence of valleys breaks up the directional bias of the streamwise wall-shear stress fluctuations. This may be due to the fact that in the valleys, the roughness elements obstruct the flow, produce more events with smaller positive τ_{yx} , and even reverse flows with negative τ_{yx} . The increased probability of occurrences with the yaw angle between 90° and 180° illustrates that the flow reversals are enhanced in the valleys, however, they are not as strong as the recirculation zones between the rods where the probability for Case RRW is even larger. As Re_τ increases, the p.d.f. profile of the valley region in Case R600 becomes more evenly distributed. Compared to Case R400, the probability of events with $0^\circ < |\phi_\tau| < 70^\circ$ is decreased, while the probability of events with $70^\circ < |\phi_\tau| < 180^\circ$ increases, implying that the reverse flows are enhanced as Re_τ increases.

4.2.2. Joint p.d.f. distribution of wall-shear stress

Figure 21 shows the joint p.d.f. of the wall shear-stress vector magnitude and the yaw angle for the smooth, rod-roughened, and random-rough cases. The joint p.d.f. of Case SW in figure 21(a) shows a similar contour map as Diaz-Daniel *et al.* (2017), who found that the probability of events with very small shear-stress magnitude $||\tau||$ can be neglected, and the probability is maximum when the shear-stress vector is parallel to the flow direction. A completely different distribution can be seen for Case RRW, as shown in figure 21(b). First, the probability of events with small shear-stress magnitude is not negligible, supporting the view that due to the existence of roughness elements, small τ_{yx} can be strongly correlated with small τ_{yz} . Second, the most significant correlation occurs at small $||\tau||$ and large $|\phi_\tau|$ close to 180° , which corresponds to the events that large and negative τ_{yx} is associated with small τ_{yz} . These results are due to the fact that the flow between two adjacent rods within a cavity is strongly dominated by the recirculations. Moreover, for Case SW, when $20^\circ < |\phi_\tau| < 40^\circ$, the probability of high magnitude events exhibits a sharp decrease. In contrast, a similar trend is observed in Case RRW but the probability is quite low, thus the contour does not show more detail.

Case R400 also presents interesting features in figure 21(c). First, the events with shear-stress magnitude close to zero have a higher and more uniform probability than those of Case RRW, covering the range from small yaw angle (0°) to large yaw angle (180°). This may result from the fact that, for the random-rough case, the roughness elements are more homogeneously distributed, thus the reverse flow is not induced as strong as that in Case RRW, and the correlation between small τ_{yx} and small τ_{yz} has no significant bias in $|\phi_\tau|$. Second, the maximum probability occurs at $|\phi_\tau| = 0$, similar as Case SW, however, it shifts to a smaller shear-stress magnitude. The corresponding events of zero $|\phi_\tau|$ and small $||\tau||$ are small magnitude of wall-shear stress with relatively larger τ_{yx} and small τ_{yz} , which are consistent with the features of low-speed streaks in the streamwise direction. Since the random roughness can break up the streaks into small-scale structures, this maximum probability could happen at a smaller magnitude of wall-shear stress. Additionally, the distribution maintains similar features with Case SW when $|\phi_\tau|$ is small, but is spread over a larger shear-stress magnitude. This is because that the streamwise velocity increases as the wall-normal distance goes away from the

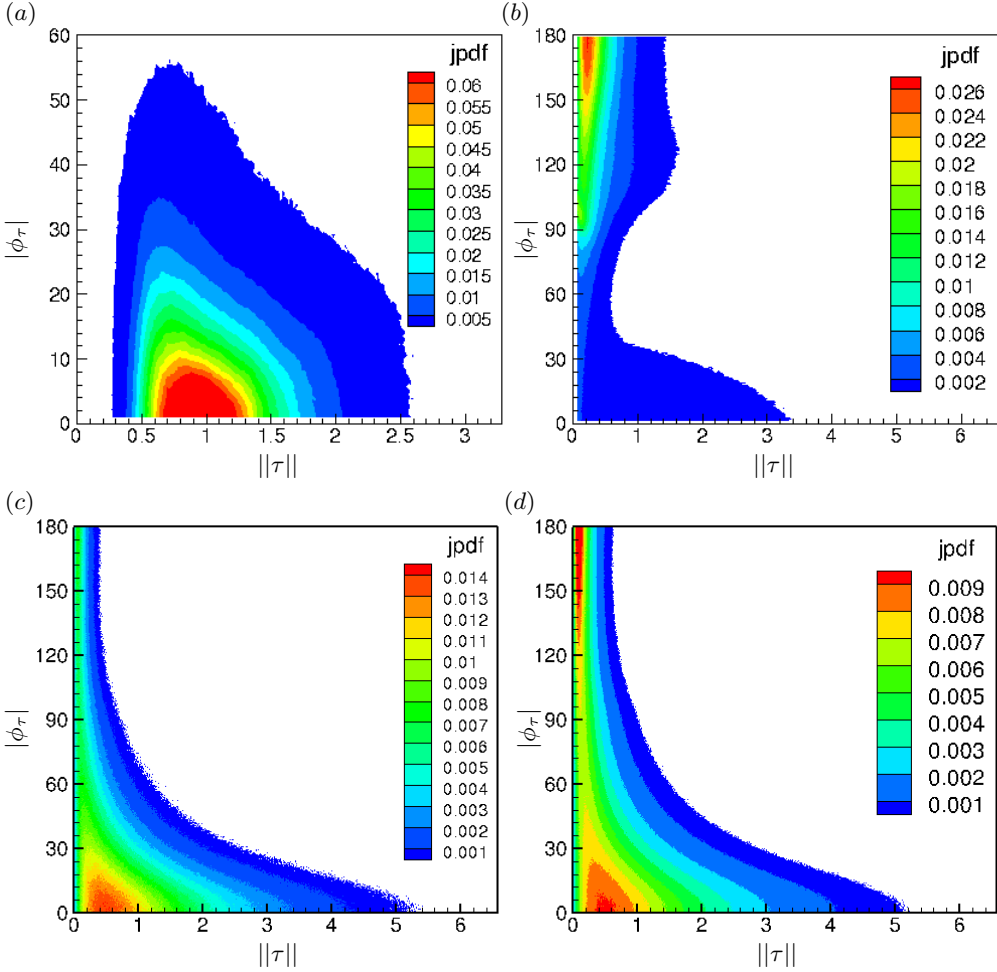


FIGURE 21. Joint p.d.f. distribution of the norm and yaw angle of the wall shear-stress vector: (a) Case SW, (b) Case RRW, (c) Case R400 and (d) Case R600. The contour map is shown in the different range for different cases, and has a cut-off below the probability 0.0005.

wall. A similar distribution is observed in Case R600, shown in figure 21(d). There are mainly two differences presented between Case R400 and Case R600. One is that the joint p.d.f. contour range is diminished at higher Re_τ . This is due to the fact that the level of wall-shear stress fluctuations is enhanced as Re_τ increases, thus the range of $||\tau||$ at $Re_\tau = 600$ is larger than that at $Re_\tau = 400$. This is not shown in figure 21 since the contour map is cut off below the probability 0.0005. The other noticeable difference is that the maximum correlation occurs at large $|\phi_\tau|$ in Case R600, which indicates that the reverse flow is enhanced in the random-rough case as Re_τ increases, consistent with the results shown in figure 19.

In order to obtain a better understanding of the joint p.d.f. distribution for the rough cases, the results are investigated based on separate regions. As shown in figure 22(a), the joint p.d.f. distribution of wall-shear stress on the top surface of rods has a similar shape with the smooth wall. However, the distribution is extended in both $||\tau||$ and $|\phi_\tau|$ than that of Case SW. The enhanced probability at larger $||\tau||$ is because that the wall-shear stress is strongly correlated with the streamwise velocity. The joint p.d.f. of the bottom

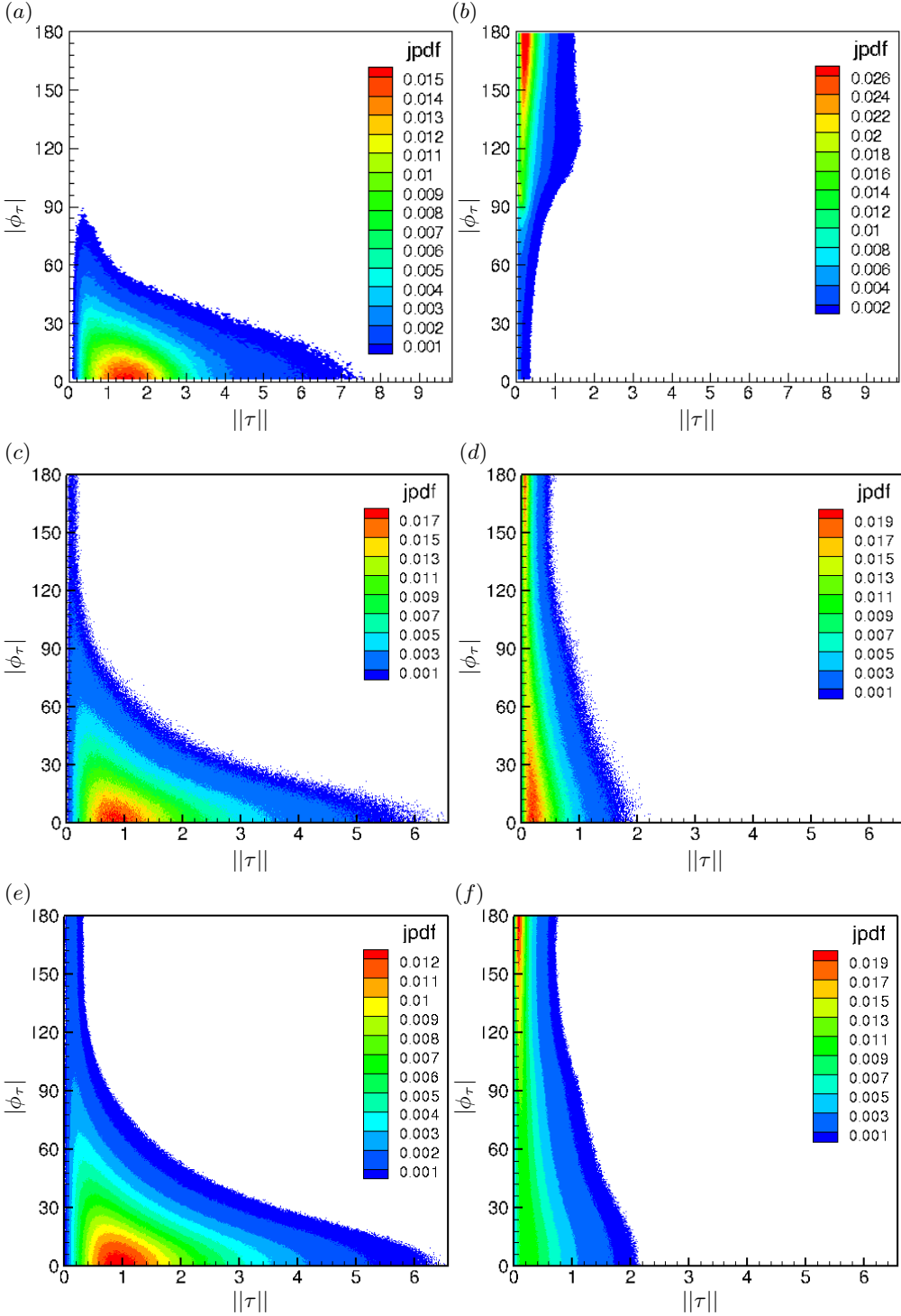


FIGURE 22. Joint p.d.f. distribution of the norm and yaw angle of the wall shear-stress vector for separate regions: (a) the top surface of the rods and (b) the bottom surface in the cavity in Case RRW, (c) the peak region and (d) the valley region in Case R400, (e) the peak region and (f) the valley region in Case R600. The contour map is shown in the different range for different cases, and has a cut-off below the probability 0.0005.

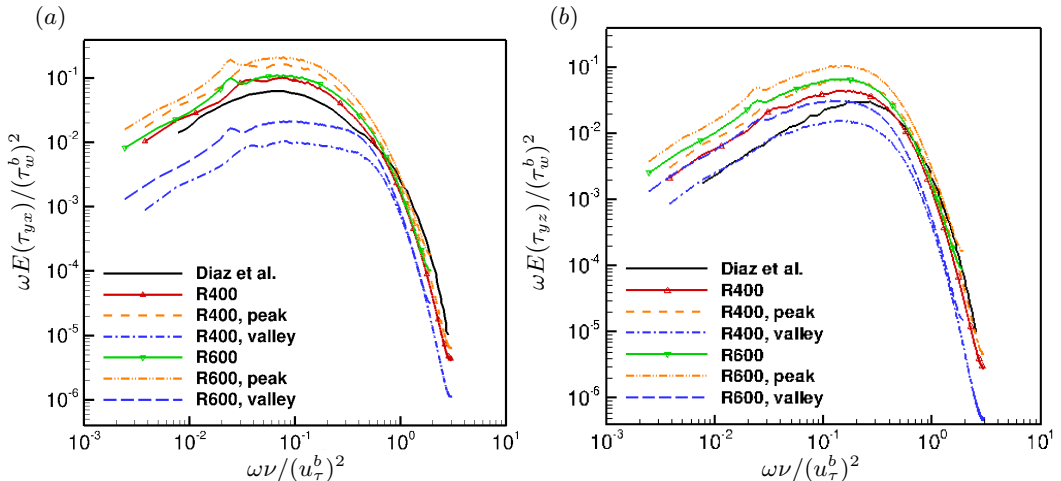


FIGURE 23. Temporal energy spectrum of (a) streamwise wall-shear stress τ_{yx} and (b) spanwise wall-shear stress τ_{yz} for Case R400 and Case R600 compared to the results of a smooth turbulent boundary layer from Diaz-Daniel *et al.* (2017).

surface in Case RRW is shown in figure 22(b), where the maximum probability at large $|\phi_\tau|$ represents the reverse flow in the cavity. Combining these two distributions gives us an explanation of the joint p.d.f. on the overall surface in figure 21(b).

For Case R400, figure 22(c) shows that the peak region has a higher probability for events with small $\|\tau\|$ and large $|\phi_\tau|$ compared to the top surface of Case RRW. This difference is contributed by the flow within the roughness layer and indicates that the reverse flow mainly exists in the roughness region. The results in the valley region, as shown in figure 22(d), demonstrate that the events with small shear-stress magnitude $\|\tau\| < 2$ and large yaw angle $90^\circ < |\phi_\tau| < 180^\circ$ have a relatively even-distributed and smaller probability, compared to those of the bottom surface in Case RRW. The maximum probability is concentrated in the region of small $\|\tau\|$ and small $|\phi_\tau|$. The reverse flow is mainly induced by the presence of valleys. Considering that Case RRW and Case R400 have the similar roughness height in wall units, these observations can be attributed to the difference in roughness type. The random roughness is three-dimensional, irregular roughness while the rod-roughened surface is two-dimensional roughness and uniform in the spanwise direction, thus the vortices induced within the roughness valleys in Case R400 is not as strong as that in Case RRW. The peak region of Case R600 has a similar distribution as Case R400, shown in figure 22(e). The only difference is that the contour legend has a smaller range because the magnitude of wall-shear stress is increased. In the valley region of Case R600, shown in figure 22(f), the maximum probability of the joint p.d.f. corresponds to large yaw angles, suggesting that higher Re_τ enhances the reverse flow in the valleys.

4.2.3. Wall-shear stress spectrum

The temporal energy spectra of the wall-shear stress components $E_{\tau_{yx}}$ and $E_{\tau_{yz}}$ are shown in figure 23. The time histories were obtained along the rough surface in a time period $T^+ = 6400$ with a time interval $t^+ = tu_\tau/\nu = 1$, which gives a minimum frequency of $\omega\nu/(u_\tau^b)^2 = 0.004$, and a maximum frequency of $\omega\nu/(u_\tau^b)^2 = 3.14$. To improve the statistical convergence of the energy spectrum, the time period was split and windowed in 7 blocks with 50% overlap, which gives a frequency resolution of $\Delta\omega = 1.56$ ($\Delta\omega^+ = 3.9 \times 10^{-3}$ at $Re_\tau = 400$ and $\Delta\omega^+ = 2.6 \times 10^{-3}$ at $Re_\tau = 600$). The temporal energy

spectra were computed for each projected surface cell and averaged by the number of cells. In the plots, the energy spectra is multiplied by the frequency ω and normalized by $(\tau_w^b)^2$ of the rough wall for the rough cases, where $(\tau_w^b)^2 = 1.04$ for Case R400 and $(\tau_w^b)^2 = 1.15$ for Case R600.

The energy spectra of τ_{yx} and τ_{yz} of the overall rough surface, as well as the peak and valley regions are investigated in figure 23(a) and (b). The results are compared to the DNS data at $Re_\theta = 1090$ (approximately corresponding to $Re_\tau = 400$) of a zero pressure-gradient smooth-wall turbulent boundary layer from Diaz-Daniel *et al.* (2017). The energy spectra on the rough walls have a generally similar profile to those computed on the smooth wall: a rise at low frequencies, a medium frequency region where the maximum energy spectra occur, and a rapid roll off at high frequencies. Some important differences are noted upon more detailed comparison. The energy spectra of the overall rough surface shows that the low and medium frequencies contain more energy compared to those of the smooth wall, indicating that the large turbulence scales have a higher energy in the rough cases. After the frequency is normalized by $(u_\tau^b)^2$ for the rough wall, the maximum spectra of the streamwise component appears at the same frequency $\omega^+ = 0.07$ as the smooth wall, while the maximum spectra of the spanwise component occurs at a lower frequency $\omega^+ = 0.15$ compared to $\omega^+ = 0.26$ in the smooth case. The peak of the premultiplied energy spectra is associated with the size of the streamwise streaks, suggested by Hutchins & Marusic (2007). In light of this relation, Diaz-Daniel *et al.* (2017) infers that the peak frequency could indicate the most energetic turbulence scales. According to their suggestions, the most energetic turbulence scales are maintained in the rough case, however, a general rise in energy occurs at low and medium frequencies. In the mid-frequency range after the spectral peak, the rough-wall shear stress spectrum begins a roll-off at high frequencies due to dissipation with a noticeably higher slope. This sharper decline results in a less energy in the high-frequency region, where the profile of the streamwise component presents a more obvious decrease than that of the spanwise component.

The energy spectra of wall-shear stress are also examined separately in the peak and valley regions. For both streamwise and spanwise wall-shear stress components, the spectra of the peak region shows that the low and medium frequencies contain an even higher energy than those of the overall surface. The spectra at high frequencies is slightly higher than that of the overall surface with an approximately identical slope of decline. The valley regions have more significant differences between the spectra of τ_{yx} and τ_{yz} . The valley region of the streamwise component presents a more noticeable decrease at low and medium frequencies, indicating that the energy of large turbulence scale is strongly damped out in the valleys of the roughness elements. This is consistent with the concentrated distribution of joint p.d.f. at small magnitude of wall-shear stress in the valley regions, as shown in figure 22. However, the spectra of the valley region has a more moderate decrease at high frequencies, which suggests that even though the energy of small turbulence scales is decreased, the roughness effect on it is less significant than that on the energy of large turbulent scales. Compared to the streamwise component, the spectrum of the spanwise component in the valley region has an equivalent value at low frequencies with the spectrum of the smooth-wall case, while the medium and high frequencies contain less energy. The results indicate that the roughness has a more significant effect on the wall-shear stress spectra in the streamwise direction than the spanwise direction, especially in the valley region of roughness elements. At the higher Re_τ , an obvious increase in the spectra at low and medium frequencies is observed, while the same values are maintained at high frequency, indicating that the large turbulent scales are more significantly affected and have an increased energy with increasing Re_τ .

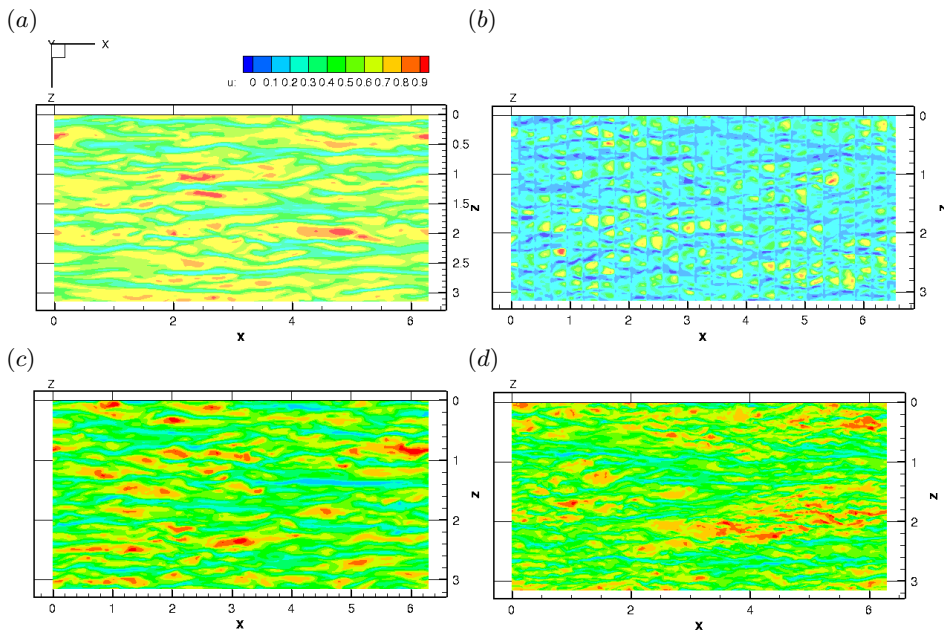


FIGURE 24. Instantaneous contours of u/u_{max} for (a) Case SW at $y^+ = 12$ (corresponding to $y = 0.03$), (b) Case RRW at $y^+ = 14.4$ ($y = 0.036$, the location above the top surface of the rods), (c) Case R400 at $y^+ = 12$ and (d) Case R600 at $y^+ = 18$ (both corresponding to $y = 0.03$, the location above the maximum height of the roughness elements). The contour range is from 0 to 0.9 in wall units.

4.3. Instantaneous flow field

4.3.1. Instantaneous velocity field

The instantaneous streamwise velocity field of the random-rough case is compared to the smooth and rod-roughened case at different y locations in figure 24 - 26. The streamwise velocity is normalized by the maximum streamwise velocity u_{max} of the y plane. Figure 24(a) shows the velocity contour at $y^+ = 12$ in the smooth-wall channel flow. The high-speed fluid formed as the streaky structures in the streamwise direction can be observed in this plane. The plane $y^+ = 14.4$ right above the crests of the rods is extracted in figure 24(b). The contour map shows that there are more low-speed areas, which indicates more drag. Both low-speed and high-speed fluid are interrupted by the rods and appear as the intermittent structures. Figure 24(c) and (d) show the instantaneous streamwise velocity field for Case R400 and Case R600 at the plane $y = 0.03$ which is the immediate vicinity beyond the edge of roughness layer. The scale of the high-speed fluids is diminished in figure 24(c), compared to that at the same y^+ of Case SW in figure 24(a). However, a higher level of fluctuations is presented in these high-speed regions. This implies that the random roughness elements break up the high-speed streaks and cause a stronger level of fluctuations, consistent with the results suggested in §4.1. For Case R600, the scale of the streaks is decreased further and the areas of the high-speed regions are reduced, resulting in a more uniform velocity field, which indicates that the roughness effect is more significant at the higher Re_τ .

Then the wall-normal distance is lowered and the velocity field within the peak region is visualized in figure 25. The planes at $y^+ = 6$ of Case SW and $y^+ = 12$ of Case RRW are extracted and compared to the location $y = 0.015$ of the random-rough cases at the two Re_τ (the corresponding $y^+ = 6$ in Case R400 and $y^+ = 9$ in Case R600). Compared

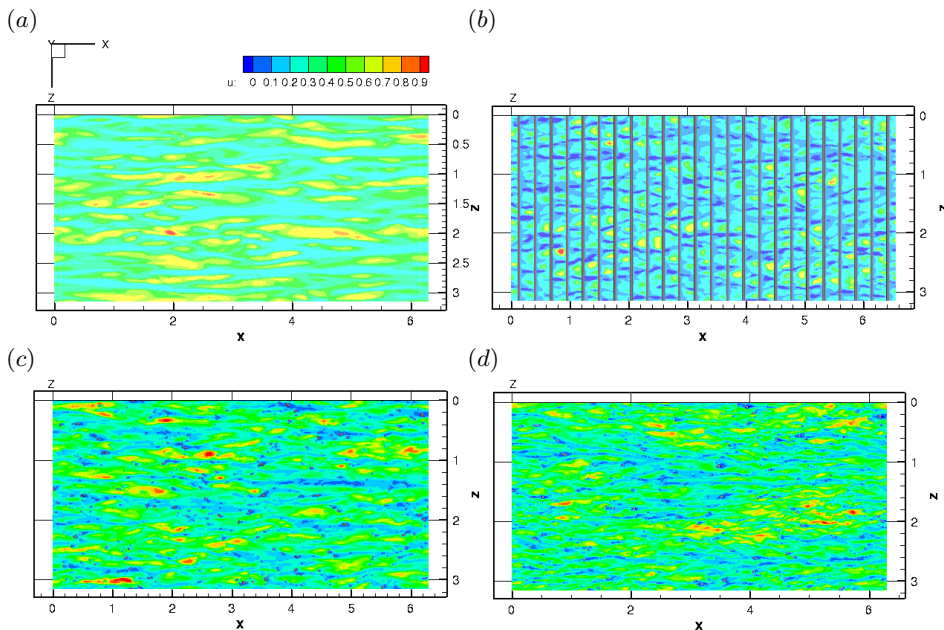


FIGURE 25. Instantaneous contours of u/u_{max} for (a) Case SW at $y^+ = 6$ (corresponding to $y = 0.015$), (b) Case RRW at $y^+ = 12$ ($y = 0.03$, the location within cavities between the rods), (c) Case R400 at $y^+ = 6$ and (d) Case R600 at $y^+ = 9$ (both corresponding to $y = 0.015$, the location in the peak region of the roughness elements). The contour range is from 0 to 0.9 in wall units.

to figure 24, the scale of high-speed streaks is significantly decreased, while the low-speed streaks are more dominant at a lower y , as shown in figure 25. This is consistent with the fact that the low-speed streaks occur closer to the wall than the high-speed streaks. Figure 25(b) shows that the low-speed fluid behaviours as the streamwise streaky structures even though they are interrupted by the rods. For Case R400, the high-speed streaks are broken up and the fluid speed is decreased by the roughness elements, shown in figure 25(c). The low-speed fluid is observed behind the protruding roughness elements, corresponding to an increased probability for the events with large yaw angles and small wall-shear stress in figure 22(c). The more significant colour variation suggests that the streamwise velocity fluctuations are enhanced by the random roughness. As Re_τ increases, the length scale of the streaky structure maintains the same in the streamwise direction but is obviously diminished in the spanwise direction, shown in figure 25(d). This explains why the p.d.f. of ϕ_τ in the peak region of Case R600 has a more even distribution.

The y plane is further lowered and the velocity field is examined within the valley region in figure 26. The contour of Case SW at $y^+ = 0.4$ does not present much difference after rearranging the contour legend from -0.1 to 0.8 in figure 26(a). Figure 26(b) shows the streamwise velocity fluctuations in Case RRW at $y^+ = 6$, where the location is within the valley and close to the bottom wall. The reverse flow is dominant and trapped between the rods, and the coherent structures in the streamwise direction observed at higher y locations no longer exist at this location. Figure 26(c) and (d) show the streamwise velocity fluctuations in Case R400 and Case R600 at $y = -0.0025$. The velocity field is more quiescent in the valley region, consistent with the evidence from §4.2 that the wall-shear stress fluctuations are smaller in the valley region than those in the peak region. The reverse flow occurs behind the roughness elements and no coherent structures can

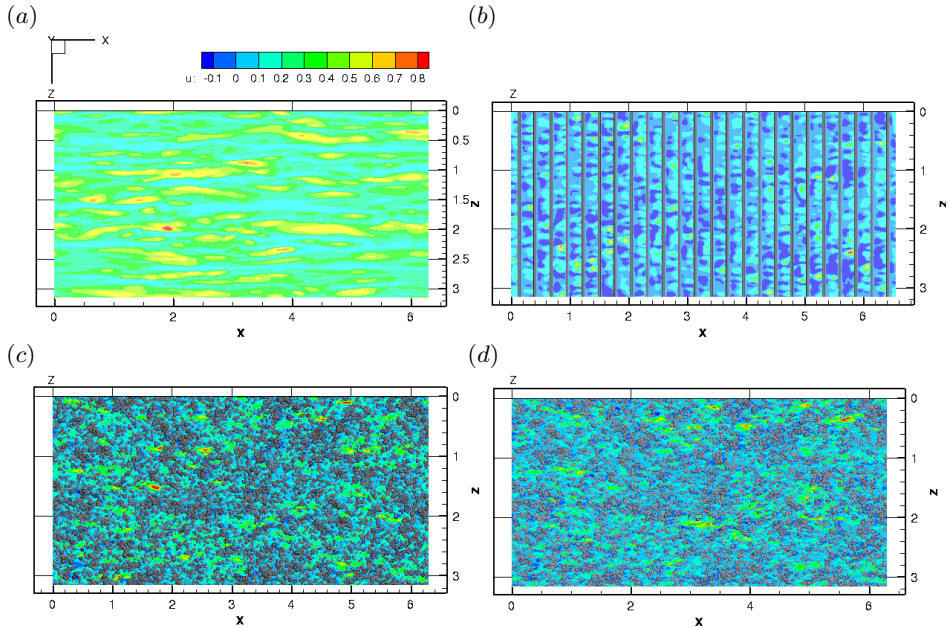


FIGURE 26. Instantaneous contours of u/u_{max} for (a) Case SW at $y^+ = 0.4$ (corresponding to $y = 0.001$), (b) Case RRW at $y^+ = 6$ ($y = 0.015$, the location above the top surface of the rods), (c) Case R400 at $y^+ = -1$ and (d) Case R600 at $y^+ = -1.5$ (both corresponding to $y = -0.0025$, the location in the valley region of the roughness elements). The contour range is from -0.1 to 0.8 in wall units.

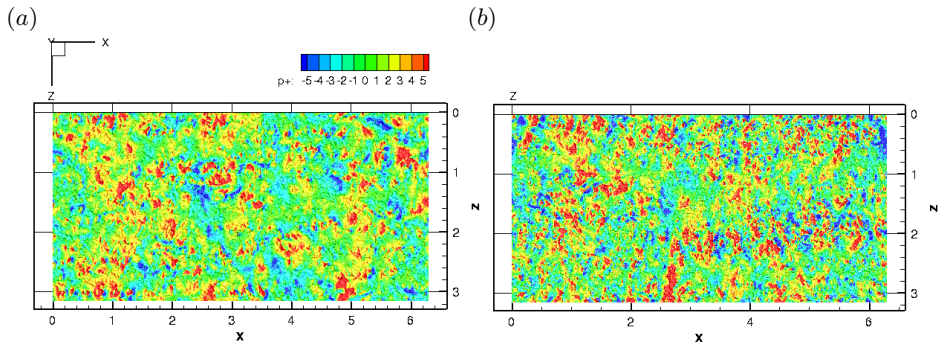


FIGURE 27. Instantaneous contours of p^+ on the rough surface for (a) Case R400 and (b) Case R600. The contour range is from -5 to 5 in wall units.

be observed in the valley region. Figure 26(d) shows that the areas of the reverse flow are increased at the higher Re_τ , verifying the probability of the events with large yaw angle is enhanced as Re_τ increases shown in §4.2.

4.3.2. Instantaneous pressure field

The results in §4.1.4 show that the pressure fluctuation is strongly enhanced in the roughness layer. The instantaneous pressure field in the near-wall region is examined in this section. Figure 27(a) and (b) show the pressure contour $p^+ = p/(u_\tau^b)^2$ along the rough surface for Case R400 and R600. The pressure field at the higher Re_τ shows smaller length scales. In figure 28, the pressure fluctuation for the random-rough cases are compared to that in Case SW at the same wall-normal location $y = 0.0075$. A more intense variation at

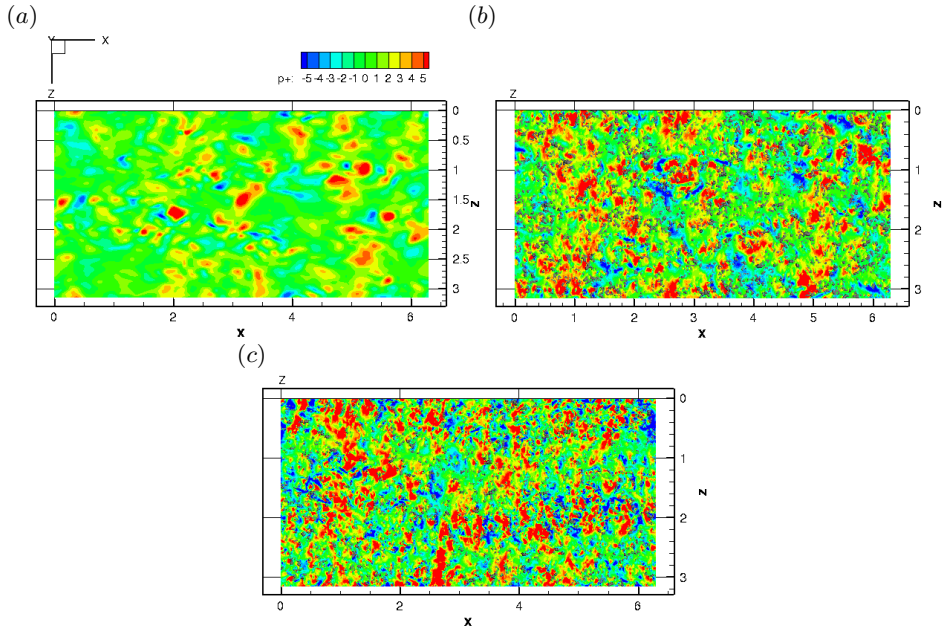


FIGURE 28. Instantaneous contours of p^+ in the roughness layer for (a) Case SW at $y^+ = 3$, (b) Case R400 at $y^+ = 3$ and (c) Case R600 at $y^+ = 4.5$ (both corresponding to $y = 0.0075$, the location above the mean height of the roughness elements). The contour range is from -5 to 5 in wall units.

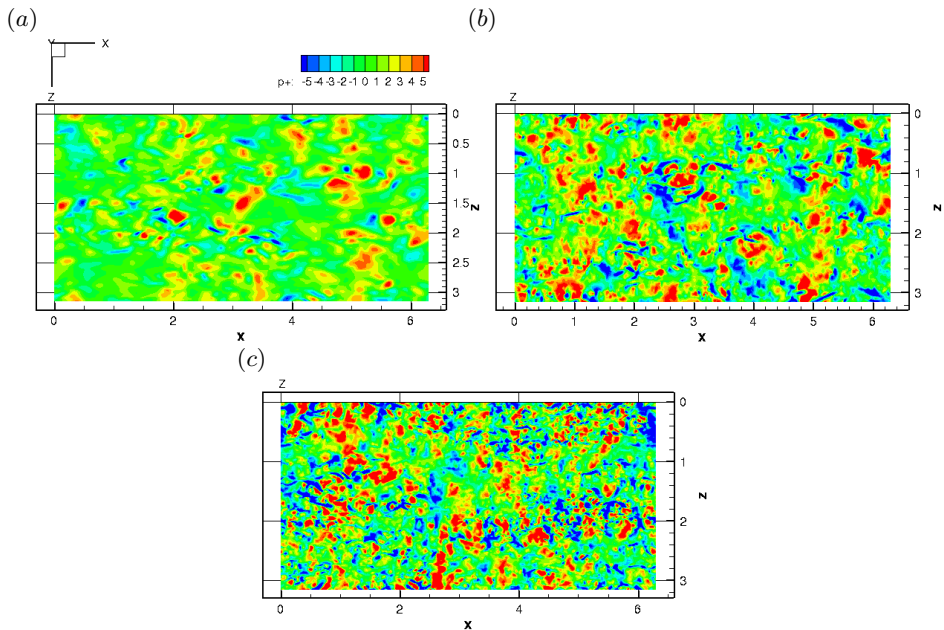


FIGURE 29. Instantaneous contours of p^+ above the roughness layer for (a) Case SW at $y^+ = 12$, (b) Case R400 at $y^+ = 12$ and (c) Case R600 at $y^+ = 18$ (both corresponding to $y = 0.03$, the location above the maximum height of the roughness elements). The contour range is from -5 to 5 in wall units.

smaller length scales is observed for the random-rough cases. The instantaneous pressure field at several time instants shows that the pressure pattern moves with the flow, similar to Case SW. However, the high-pressure regions are split into smaller scales as they pass through the asperities of the roughness elements, resulting in an enhancement in the pressure fluctuations. As Re_τ increases, the variation becomes even more intense and the pressure pattern turns into even smaller scales, corresponding to the increase in the magnitude of $\langle p'^2 \rangle^+$. At $y = 0.03$ above the roughness layer, similar behaviour is shown in figure 29. This means that the roughness effect on pressure fluctuations has extended into the region above the roughness layer.

5. Summary

DNS of turbulent channel flows over random rough surfaces is performed at $Re_\tau = 400$ and 600, where the flow is in the transitionally rough regime. The random rough surfaces are produced from the original rough tiles which are scanned from experiments (Flack and Schultz). The surface statistics of the random rough surfaces are in agreement with the original tiles. Smooth and rod-roughened channel flows at $Re_\tau = 400$ are also performed to validate the flow solver and compared to the random-rough channel flows.

The skin friction coefficient and the roughness function of the random-rough cases agree with the experimental results of Flack and Schultz (personal communication). Since the random-rough surface is only applied on the bottom wall, scaling using the local friction velocity and the effective layer thickness provides a better collapse for the profiles of Reynolds stresses. At the peak of the profile, the streamwise velocity fluctuations show decrease while the spanwise and wall-normal velocity fluctuations show increase. In the present case, where the roughness scales are quite small, the streamwise and spanwise velocity fluctuations are enhanced prominently on the rough wall, while the wall-normal velocity fluctuations and Reynolds shear stress are affected slightly. The velocity field shows that the random roughness breaks up the high-speed streaks and enhances the velocity fluctuations. The scales of streaks are diminished at higher Re_τ , resulting in a more uniform flow field with increased areas of reverse flow in the valley regions.

The mean-square pressure is enhanced in the roughness layer. The profile collapses well with that of smooth cases in the outer layer, following the logarithmic law. As Re_τ increases, the roughness effects on pressure fluctuations are enhanced but the enhancement is restricted to the near-wall region. The pressure field of the random-rough case shows that the scales of high-pressure and low-pressure regions are the same compared to those of the smooth case at the same Re_τ , but the variation is more intense. The scales of high-pressure and low-pressure regions becomes smaller at higher Re_τ . These effects shown in the pressure field extend into the region above the roughness layer, which is consistent with the result of mean-square pressure profiles.

Roughness effects on streamwise mean momentum balance are examined. The pressure gradient is induced by the roughness elements and disappears above the roughness layer. The viscous stress gradient is enhanced in the roughness layer and has a large magnitude in the valley region of the roughness. The layer structure of MMB is generally maintained in the random-rough cases, however, two important differences are noted. First, the ratio of the viscous to the Reynolds stress gradients becomes large and positive, attributed to the enhancement of the viscous stress gradient in the roughness layer. Second, the transition of the ratio switching its sign occurs closer to the rough wall, implying the peak of Reynolds stress moving closer to the rough wall.

The statistics of wall-shear stress fluctuations are investigated respectively in two regions for the rod-roughened and random-rough cases, and compared to those in the

smooth case. The following conclusions are drawn: (i) only τ_{yx} on the bottom surface of the rod-roughened case shows a negative skewness since the strong recirculation is located in the cavity, (ii) the probability of negative τ_{yx} in the valley region is higher than that in the peak region and the smooth wall, indicating that the reverse flow is enhanced by the random roughness and mainly occurs in the valley region, and (iii) the p.d.f. has a better collapse after the wall-shear stress fluctuations are subtracted by the mean and normalized by the rms value. The random-rough cases show a widened range and an increased value in the tails of the p.d.f. profiles. These observations are consistent with the increased kurtosis, meaning that the probability of extreme events are enhanced by the random roughness. These roughness effects are also enhanced with increasing Re_τ .

The joint p.d.f. of the norm and yaw angle of the wall-shear stress vector is also investigated in different regions for rough cases. The results are summarized as follows: (i) the correlation between large magnitude of wall-shear stress and small yaw angles is increased in the peak region since the streamwise velocity becomes larger as the wall-normal distance increases, (ii) the correlation between small magnitudes and large yaw angles cannot be neglected in the peak region, corresponding to the fact that the reverse flow is induced within the roughness elements, and (iii) the strongest correlation in the valley region of the random-rough case is at small yaw angles, however, it converts to large yaw angles at higher Re_τ . This suggests that the reverse flow of the random-rough case is not strong as the recirculations in the rod-roughened case, but higher Re_τ enhances the reverse flow in the valleys. Finally, the temporal energy spectra of wall-shear stresses for the random-rough cases show that the most energetic turbulent scales maintain the same as those in the smooth channel flows. The low and medium frequencies contain more energy while the high frequencies show a larger slope of decline and contain slightly less energy, compared to those in the smooth case.

Acknowledgements

This work was supported by the United States Office of Naval Research (ONR) Grant N00014-17-1-2308 managed by Drs. J. Gorski, T. Fu and P. Chang. Computing resources were provided by the Minnesota Supercomputing Institute (MSI). We are grateful to Professor K. Flack at the United States Naval Academy for providing us with the scanned surface data used in the present work. The authors would like to thank Mr. S. Anantharamu, Dr. P. Kumar and Dr. Y. Li for their helpful discussions and suggestions.

REFERENCES

- ABE, H., KAWAMURA, H. & CHOI, H. 2004 Very large-scale structures and their effects on the wall shear-stress fluctuations in a turbulent channel flow up to $Re_\tau = 640$. *J. Fluids Eng.* **126** (5), 835–843.
- ALAMÉ, K. & MAHESH, K. 2019 Wall-bounded flow over a realistically rough superhydrophobic surface. *J. Fluid Mech.* **873**, 977–1019.
- ALFREDSSON, P. H., JOHANSSON, A. V., HARITONIDIS, J. H. & ECKELMANN, H. 1988 The fluctuating wall-shear stress and the velocity field in the viscous sublayer. *Phys. Fluids* **31** (5), 1026–1033.
- ANDERSON, W., BARROS, J. M., CHRISTENSEN, K. T. & AWASTHI, A. 2015 Numerical and experimental study of mechanisms responsible for turbulent secondary flows in boundary layer flows over spanwise heterogeneous roughness. *J. Fluid Mech.* **768**, 316–347.
- ASHRAFIAN, A., ANDERSSON, H. I. & MANHART, M. 2004 DNS of turbulent flow in a rod-roughened channel. *Int. J. Heat Fluid Fl.* **25** (3), 373–383.
- BARROS, J. M., SCHULTZ, M. P. & FLACK, K. A. 2017 Measurements of skin-friction

- of systematically generated surface roughness. In *10th International Symposium on Turbulence and Shear Flow Phenomena (TSFP10), Chicago, USA*.
- BECHERT, D. W., BRUSE, M., HAGE, W., VAN DER HOEVEN, J. G. T. & HOPPE, G. 1997 Experiments on drag-reducing surfaces and their optimization with an adjustable geometry. *J. Fluid Mech.* **338**, 59–87.
- BHAGANAGAR, K., COLEMAN, G. & KIM, J. 2007 Effect of roughness on pressure fluctuations in a turbulent channel flow. *Phys. Fluids* **19** (2), 028103.
- BONS, J. P., TAYLOR, R. P., MCCCLAIN, S. T. & RIVIR, R. B. 2001 The many faces of turbine surface roughness. In *ASME turbo expo 2001: Power for land, sea, and air*, pp. V003T01A042–V003T01A042. American Society of Mechanical Engineers.
- BUSSE, A., LÜTZNER, M. & SANDHAM, N. D. 2015 Direct numerical simulation of turbulent flow over a rough surface based on a surface scan. *Comput. Fluids* **116**, 129–147.
- BUSSE, A., THAKKAR, M. & SANDHAM, N. D. 2017 Reynolds-number dependence of the near-wall flow over irregular rough surfaces. *J. Fluid Mech.* **810**, 196–224.
- CARDILLO, J., CHEN, Y., ARAYA, G., NEWMAN, J., JANSEN, K. & CASTILLO, L. 2013 DNS of a turbulent boundary layer with surface roughness. *J. Fluid Mech.* **729**, 603–637.
- CHAMBERS, F. W., MURPHY, H. D. & MCELIGOT, D. M. 1983 Laterally converging flow. part 2. temporal wall shear stress. *J. Fluid Mech.* **127**, 403–428.
- CHENG, H. & CASTRO, I. P. 2002 Near wall flow over urban-like roughness. *Bound.-Layer. Meteor.* **104** (2), 229–259.
- COCEAL, O., THOMAS, T. G., CASTRO, I. P. & BELCHER, S. E. 2006 Mean flow and turbulence statistics over groups of urban-like cubical obstacles. *Bound.-Layer. Meteorol.* **121** (3), 491–519.
- DE MARCHIS, M., NAPOLI, E. & ARMENIO, V. 2010 Turbulence structures over irregular rough surfaces. *J. Turbul.* **11** (3), N3.
- DIAZ-DANIEL, C., LAIZET, S. & VASSILICOS, J. C. 2017 Wall shear stress fluctuations: Mixed scaling and their effects on velocity fluctuations in a turbulent boundary layer. *Phys. Fluids* **29** (5), 055102.
- ECKELMANN, H. 1974 The structure of the viscous sublayer and the adjacent wall region in a turbulent channel flow. *J. Fluid Mech.* **65** (3), 439–459.
- FLACK, K. A. & SCHULTZ, M. P. 2010 Review of hydraulic roughness scales in the fully rough regime. *J. Fluids Eng.* **132** (4), 041203.
- FLACK, K. A., SCHULTZ, M. P. & SHAPIRO, T. A. 2005 Experimental support for Townsend's Reynolds number similarity hypothesis on rough walls. *Phys. Fluids* **17** (3), 035102.
- HU, Z., MORFEY, C. L. & SANDHAM, N. D. 2006 Wall pressure and shear stress spectra from direct simulations of channel flow. *AIAA J.* **44** (7), 1541–1549.
- HUTCHINS, N. & MARUSIC, I. 2007 Large-scale influences in near-wall turbulence. *Philos. T. R. Soc. A* **365** (1852), 647–664.
- JELLY, T. O. & BUSSE, A. 2018 Reynolds and dispersive shear stress contributions above highly skewed roughness. *J. Fluid Mech.* **852**, 710–724.
- JEON, S., CHOI, H., YOO, J. Y. & MOIN, P. 1999 Space-time characteristics of the wall shear-stress fluctuations in a low-Reynolds-number channel flow. *Phys. Fluids* **11** (10), 3084–3094.
- JIMÉNEZ, J. 2004 Turbulent flows over rough walls. *Annu. Rev. Fluid Mech.* **36**, 173–196.
- KHOO, B. C., CHEW, Y. T. & TEO, C. J. 2001 Near-wall hot-wire measurements. *Exp. Fluids* **31** (5), 494–505.
- KIRSCHNER, C. M. & BRENNAN, A. B. 2012 Bio-inspired antifouling strategies. *Annu. Rev. Mater. Res.* **42**, 211–229.
- LEE, J. H., SUNG, H. J. & KROGSTAD, P. 2011 Direct numerical simulation of the turbulent boundary layer over a cube-roughened wall. *J. Fluid Mech.* **669**, 397–431.
- LENAERS, P., LI, Q., BRETHOUWER, G., SCHLATTER, P. & ÖRLÜ, R. 2012 Rare backflow and extreme wall-normal velocity fluctuations in near-wall turbulence. *Phys. Fluids* **24** (3), 035110.
- LIGRANI, P. M. & MOFFAT, R. J. 1986 Structure of transitionally rough and fully rough turbulent boundary layers. *J. Fluid Mech.* **162**, 69–98.
- LOZANO-DURÁN, A. & JIMÉNEZ, J. 2014 Effect of the computational domain on direct simulations of turbulent channels up to $Re_\tau = 4200$. *Phys. Fluids* **26** (1), 011702.

- MADAVAN, N. K., DEUTSCH, S. & MERKLE, C. L. 1985 Measurements of local skin friction in a microbubble-modified turbulent boundary layer. *J. Fluid Mech.* **156**, 237–256.
- MAHESH, K., CONSTANTINESCU, G. & MOIN, P. 2004 A numerical method for large-eddy simulation in complex geometries. *J. Comput. Phys.* **197** (1), 215–240.
- MEHDI, F., KLEWICKI, J. C. & WHITE, C. M. 2010 Mean momentum balance analysis of rough-wall turbulent boundary layers. *Physica D* **239** (14), 1329–1337.
- MEJIA-ALVAREZ, R. & CHRISTENSEN, K. T. 2010 Low-order representations of irregular surface roughness and their impact on a turbulent boundary layer. *Phys. Fluids* **22** (1), 015106.
- MEYERS, T., FOREST, J. B. & DEVENPORT, W. J. 2015 The wall-pressure spectrum of high-Reynolds-number turbulent boundary-layer flows over rough surfaces. *J. Fluid Mech.* **768**, 261–293.
- MIGNOT, E., BARTHÉLEMY, E. & HURTHER, D. 2009 Double-averaging analysis and local flow characterization of near-bed turbulence in gravel-bed channel flows. *J. Fluid Mech.* **618**, 279–303.
- MOSER, R. D., KIM, J. & MANSOUR, N. N. 1999 Direct numerical simulation of turbulent channel flow up to $Re_\tau = 590$. *Phys. Fluids* **11** (4), 943–945.
- NIKURADSE, J. 1933 Laws of flow in rough pipes. national advisory committee for aeronautics. *NACA Technical Memorandum, NACA Technical Memorandum* **1292**, 60–68.
- ORLANDI, P. & LEONARDI, S. 2006 DNS of turbulent channel flows with two-and three-dimensional roughness. *J. Turbul.* **7** (53), N73.
- ÖRLÜ, R. & SCHLATTER, P. 2011 On the fluctuating wall-shear stress in zero pressure-gradient turbulent boundary layer flows. *Phys. Fluids* **23** (2), 021704.
- PANTON, R. L., LEE, M. & MOSER, R. D. 2017 Correlation of pressure fluctuations in turbulent wall layers. *Phys. Rev. Fluids* **2** (9), 094604.
- POPE, S. B. 2001 Turbulent flows.
- RAUPACH, M. R., ANTONIA, R. A. & RAJAGOPALAN, S. 1991 Rough-wall turbulent boundary layers. *Appl. Mech. Rev.* **44** (1), 1–25.
- SCHLICHTING, H. 1936 Experimentelle untersuchungen zum rauhgigkeitsproblem. *Arch. Appl. Mech.* **7** (1), 1–34.
- SCHULTZ, M. P. & FLACK, K. A. 2013 Reynolds-number scaling of turbulent channel flow. *Phys. Fluids* **25** (2), 025104.
- WEI, T., FIFE, P., KLEWICKI, J. & MCMURTRY, P. 2005 Properties of the mean momentum balance in turbulent boundary layer, pipe and channel flows. *J. Fluid Mech.* **522**, 303–327.
- WU, Y. & CHRISTENSEN, K. T. 2007 Outer-layer similarity in the presence of a practical rough-wall topography. *Phys. Fluids* **19** (8), 085108.
- YUAN, J. & JOUYBARI, M. A. 2018 Topographical effects of roughness on turbulence statistics in roughness sublayer. *Phys. Rev. Fluids* **3** (11), 114603.
- YUAN, J. & PIOMELLI, U. 2014 Estimation and prediction of the roughness function on realistic surfaces. *J. Turbul.* **15** (6), 350–365.